Inertial migration of deformable droplets in a microchannel

Xiaodong Chen, Chundong Xue, Li Zhang, Guoqing Hu, Xingyu Jiang, and Jiashu Sun

Articles you may be interested in

Moving towards the cold region or the hot region? Thermocapillary migration of a droplet attached on a horizontal substrate
Phys. Fluids 26, 092102 (2014); 10.1063/1.4894077

A numerical study of droplet trapping in microfluidic devices
Phys. Fluids 26, 032002 (2014); 10.1063/1.4867251

Droplet formation in microfluidic cross-junctions
Phys. Fluids 23, 082101 (2011); 10.1063/1.3615643

On the effects of liquid-gas interfacial shear on slip flow through a parallel-plate channel with superhydrophobic grooved walls
Phys. Fluids 22, 102002 (2010); 10.1063/1.3493641

Thermally mediated breakup of drops in microchannels
Appl. Phys. Lett. 89, 234101 (2006); 10.1063/1.2400200

Inertial migration of deformable droplets in a microchannel

Xiaodong Chen,[1] Chundong Xue,[1] Li Zhang,[2] Guoqing Hu,[1,a)]
Xingyu Jiang,[3] and Jiashu Sun[3,a)]

[1]*State Key Laboratory of Nonlinear Mechanics, Institute of Mechanics,
Chinese Academy of Sciences, Beijing 100190, China*
[2]*Research and Development Center, Synfuels China Technology Co., Ltd.,
Beijing 101407, China*
[3]*Beijing Engineering Research Center for BioNanotechnology and Key Lab for Biological
Effects of Nanomaterials and Nanosafety, National Center for Nanoscience and Technology,
Beijing 100190, China*

The microfluidic inertial effect is an effective way of focusing and sorting droplets
suspended in a carrier fluid in microchannels. To understand the flow dynamics of mi-
croscale droplet migration, we conduct numerical simulations on the droplet motion
and deformation in a straight microchannel. The results are compared with prelimi-
nary experiments and theoretical analysis. In contrast to most existing literature, the
present simulations are three-dimensional and full length in the streamwise direction
and consider the confinement effects for a rectangular cross section. To thoroughly
examine the effect of the velocity distribution, the release positions of single droplets
are varied in a quarter of the channel cross section based on the geometrical symme-
tries. The migration dynamics and equilibrium positions of the droplets are obtained
for different fluid velocities and droplet sizes. Droplets with diameters larger than
half of the channel height migrate to the centerline in the height direction and two
equilibrium positions are observed between the centerline and the wall in the width
direction. In addition to the well-known Segré-Silberberg equilibrium positions, new
equilibrium positions closer to the centerline are observed. This finding is validated
by preliminary experiments that are designed to introduce droplets at different ini-
tial lateral positions. Small droplets also migrate to two equilibrium positions in
the quarter of the channel cross section, but the coordinates in the width direction
are between the centerline and the wall. The equilibrium positions move toward the
centerlines with increasing Reynolds number due to increasing deformations of the
droplets. The distributions of the lift forces, angular velocities, and the deformation
parameters of droplets along the two confinement direction are investigated in detail.
Comparisons are made with theoretical predictions to determine the fundamentals of
droplet migration in microchannels. In addition, existence of the inner equilibrium
position is linked to the quartic velocity distribution in the width direction through a
simple model for the slip angular velocities of droplets. © *2014 AIP Publishing LLC*.
[http://dx.doi.org/10.1063/1.4901884]

I. INTRODUCTION

Inertial migration of spherical solid particles, droplets, and bubbles in a Poiseuille flow has
attracted considerable interest after the Segré-Silberberg effect[1,2] was discovered. This effect, which
has been verified by follow-up experimental[3–5] and theoretical[6,7] works, induces the migration
of neutrally buoyant spherical particles in pipe flows to an annulus at approximately 0.6 of the

---

a)Authors to whom correspondence should be addressed. Electronic addresses: guoqing.hu@imech.ac.cn and
sunjs@nanoctr.cn.

pipe radius. It was well-known that shear- and wall-induced forces balance particles to equilibrium positions. The shear-induced force arises from the curvature of the flow velocity profile and tends to cause migration in the direction of increasing (absolute) shear rate. The wall-induced force is a result of the interaction between the particle and the lateral wall, which drives the particle toward the centerline.[6]

In contrast to particles, the lift forces experienced by droplets are further complicated by deformation and internal fluid circulation. The flow velocity and droplet deformation as well as the ratios of density, viscosity and the size between the droplets and the surrounding flow can also influence the equilibrium position. Karnis *et al.*[5] have shown experimentally, when the Reynolds number (Re) is much less than unity, that highly deformable droplets in a Poiseuille flow migrate to the centerline if the viscosity ratio of the droplet and the surrounding flow λ is low (0.0002–4.8), whereas nearly spherical droplets with high λ suspended at a position halfway between the centerline and the channel wall behave like solid particles. Their results indicate that droplets can migrate in zero Re flow (without inertia) only if they deform; thus, the migration of a deformable droplet at non-zero Re is the result of competition between deformability and inertia.[8] The theoretical analysis by Chan and Leal[9] showed that, under the Stokes flow limit (Re ≪ 1), a droplet in a two-dimensional Poiseuille flow migrated to the centerline of the channel for λ < 0.5 or λ > 10 and away from the centerline for intermediate values of 0.5 < λ < 10. The deformed shape of the droplet was derived to be a function of governing parameters. The equilibrium position, however, was not predicted because the effect of the wall was not included. Zhou and Pozrikidis[10] have simulated droplet migration in a two-dimensional Poiseuille flow using a method of interfacial dynamics. They determined that for λ = 1, the droplet migrates toward the centerline and, for λ = 10, the deformable droplets move to an equilibrium position approximately halfway between the wall and centerline. This quantitative difference in comparison with the findings of Chan and Leal[9] was attributed to the limitations of the two-dimensional numerical simulations. Using a boundary integral method, Mortazavi and Tryggvason[8] conducted simulations of a neutrally buoyant deformable droplet in a two-dimensional Poiseuille flow at finite Reynolds numbers. They determined that the motion of the droplets depends strongly on the ratio of the viscosities, λ, when Re < 1. For λ = 0.125, the droplet moved toward the centerline, whereas for λ = 1.0, it moved away from the center until halted by wall repulsion. These results are in agreement with the theoretical predictions by Chan and Leal[9] for the viscosity dependence of migration in the limit of small deformation, even though droplet size is not small. The lateral migration was determined to be very weak, and it took a significant amount of time for the droplet to move to an equilibrium position. For higher Reynolds numbers (5–50), the droplets moved to an equilibrium position approximately halfway between the centerline and the wall. Mortazavi and Tryggvason[8] indicated that the equilibrium position of the droplet with a high viscosity is further away from the wall because of the increased viscous blocking (lubrication force) on the side of the droplet facing the wall. They also determined that an increased droplet density has the same effect as decreasing the droplet viscosity; although changes in the viscosity ratio have stronger effects.

Despite the common wisdom that inertial lift forces are negligible in microfluidics, Di Carlo *et al.*[11] have indicated that the inertial forces in symmetric and asymmetric channel geometries can create continuous streams of ordered particles precisely positioned in three dimensions. This study led to an emerging field of research on inertial microfluidics for the classification and enrichment of particles and cells.[12] For example, Kuntaegowdanahalli *et al.*[13] have achieved continuous multi-particle separation using the principle of Dean-coupled inertial migration in spiral microchannels. Recently, our group designed double spiral microchannels to focus and separate particles and cells in a high-throughput manner.[14,15] For droplets, Hur *et al.*[16] have experimentally studied the inertial migration of viscous oil droplets with various viscosities in a single straight microchannel with an aspect ratio of approximately 2.3. They determined that deformable droplets occupy equilibrium positions much closer to the channel centerline than do rigid particles. The droplets were observed to shift toward the channel center as the viscosity ratio decreased from 970 to 4.6. However, for lower viscosity ratios below 4.6, the positions moved closer to the channel wall as the viscosity ratio decreased. It is worth noting that all the observations were conducted from the view of the narrow lateral face of the channel, while the positions from the view of the wide lateral face were

not explored. Stan *et al.*[17] have investigated hydrodynamic positioning of the buoyant droplets and bubbles in a single straight microchannel with an aspect ratio of 1.6. Their experiments and numerical simulations were performed at small particle Reynolds numbers to exclude the effect of both inertial and deformation-induced lift forces. They showed that the analytical model of deformation-induced lift[9] and inertial lift[6,18] cannot provide a satisfactory quantitative prediction of the lift forces because these formulas were developed for droplets or particles much smaller than the cross section of the channel. The significant enhancements of wall confinement on generating strong hydrodynamic interaction of droplets with the wall were highlighted. Stan *et al.*[19] also measured the hydrodynamic forces for droplets with diameters from one quarter to one half of the width of the channel under small particle Reynolds numbers (0.0001–0.1). Their results showed that the lift force increases with the distance from the channel center.

The positioning effect of the lift forces can be used to separate and sort droplets simply by flowing a single-stream carrier liquid. Most existing numerical simulations of droplet migration are limited to two-dimensional Poiseuille flow, although in rectangular microchannels, droplets migrate in both the width and height directions. The process of migration is much more complex under three-dimensional confinement. In this work, the inertial migration of deformable droplets in a microchannel is investigated through fully three-dimensional numerical simulations. The effects of droplet size and the velocity profile of the undisturbed flow on the migration of deformable droplets are studied for finite Reynolds numbers. Experimental observations are also performed for comparison with the obtained numerical results. The present investigation on the migration and deformation of droplets in the microchannel helps to understand the underlying droplet dynamics in practical applications. In addition, as deformable cells behave more like droplets moving in the microchannel than rigid particles,[16] the principles obtained from the present results can be of help in designing and optimizing inertial microfluidic devices for the manipulation of cells.

II. NUMERICAL MODEL

A. Numerical methods

The basis of the present study is the general numerical framework of Gerris.[20] The formulation accommodates the conservation equations for an incompressible, variable-density flow with surface tension[20]

$$\partial_t \rho + \nabla \cdot (\rho \boldsymbol{u}) = 0, \tag{1}$$

$$\rho(\partial_t \boldsymbol{u} + \boldsymbol{u} \cdot \nabla \boldsymbol{u}) = -\nabla p + \nabla \cdot (2\mu \boldsymbol{D}) + \sigma \kappa \delta_s \boldsymbol{n}, \tag{2}$$

$$\nabla \cdot \boldsymbol{u} = 0, \tag{3}$$

where $\boldsymbol{u}$ is the velocity vector, ρ the fluid density, μ the dynamic viscosity, and $\boldsymbol{D}$ the deformation tensor defined as $D_{ij} = (\partial_i u_j + \partial_j u_i)/2$. The Dirac delta function δ_s expresses the fact that the surface tension σ is concentrated on the interface. The radius of curvature of the interface is denoted by κ, and $\boldsymbol{n}$ is the unit outward vector normal to the interface.[20]

A volume-of-fluid (VOF) function $c(\boldsymbol{x}, \boldsymbol{t})$ is introduced to trace the multi-fluid interface. $c(\boldsymbol{x}, \boldsymbol{t})$ is defined as the volume fraction of a given fluid in each cell of the computational mesh. The density and viscosity can thus be written as

$$\rho(c) \equiv c\rho_1 + (1 - c)\rho_2, \tag{4}$$

$$\mu(c) \equiv c\mu_1 + (1 - c)\mu_2, \tag{5}$$

with ρ_1, ρ_2 and μ_1, μ_2 being the densities and viscosities of the first and second fluids, respectively.

According to mass continuity, the advection equation for the density takes the following form in terms of the volume fraction:

$$\partial_t c + \nabla \cdot (c\boldsymbol{u}) = 0. \tag{6}$$

A staggered temporal discretization of the volume-fraction/density and pressure leads to a scheme that is second-order accurate in time.[20] A classical time-splitting projection method is used, which requires solving a Poisson equation. To improve numerical efficiency and robustness, the discretized momentum equation is recast as a Helmholtz-type equation that can be solved by an improved, multi-level Poisson solver.[20] The resulting Crank-Nicholson discretization of the viscous terms is second-order accurate. The spatial discretization is achieved using graded octree partitioning in three dimensions. All the variables are collocated at the center of each discretized cubic volume. Consistent with the finite-volume formulation, variables are interpreted as volume-averaged values for each cell. A piecewise-linear geometrical VOF scheme generalized for octree spatial discretization is used to solve the advection equation for the volume fraction.[21] Because the original continuum-surface-force (CSF) approach[21] suffers from problematic parasitic currents,[22] the combination of a balanced-force surface tension discretization and a height-function curvature estimation[20] is used to circumvent the problem. The Courant–Friedrichs–Lewy (CFL) number is set to be 0.8 for all the simulations to ensure overall numerical stability.

The above numerical method allows for a spatially and temporally varying resolution. In addition, the local mesh refinement or coarsening in the quad/octree discretization is extremely efficient and can be performed at every time step if necessary, with minimal impact on overall performance. The interpolation of quantities on refined or coarsened cells is also relatively simple on the regular Cartesian mesh and is achieved conservatively for both the momentum and the volume fraction.[20] In the present paper, a gradient-based adaptive mesh refinement (AMR) method is used for the volume fraction. Adequate mesh refinement is guaranteed along the entire interface where the volume fraction has gradients. Due to the confinement of the channel walls, thin films between the walls and the droplet exist when droplets are close to the walls. The efficient thickness-based refinement methods in previous study[23] are applied to refine the thin regions. The numerical methods have been validated in high-fidelity numerical simulation of impinging jet atomization.[24]

B. Simulation setup

A single droplet moving with the surrounding fluid in a rectangular microchannel is of interest (Figure 1). Gravity is neglected as an acceptable simplification in microfluidics. Dimensional analysis results in six independent, non-dimensional parameters. They are the Reynolds number, Weber
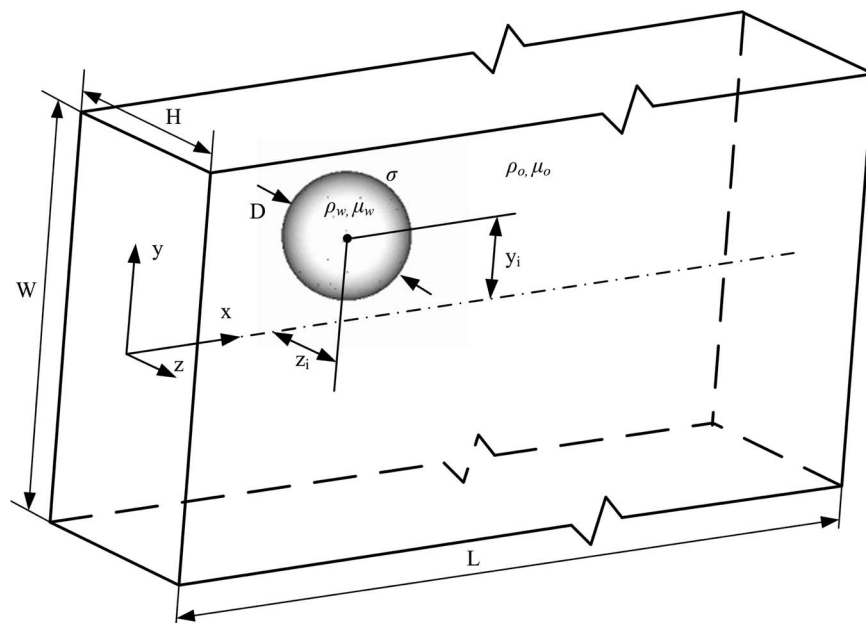

FIG. 1. Schematic illustration of a droplet in a pressure-driven flow through a microchannel with rectangular cross section.

TABLE I. Physical parameters used in the present study (at 25 °C).

H (μm)	W (μm)	L (mm)	D (μm)	ρ_w (kg/m^3)	ρ_o (kg/m^3)	μ_w (mPa s)	μ_o (mPa s)	σ (mN/m)
50	100	24	15, 30	998	768	1	3	10

number, ratio of the height to the width of the channel, ratio of the droplet diameter to the height of the channel, and the ratio of the densities and viscosities of water and oil, defined as $\text{Re} = \rho_o U_a D / \mu_o$, $\text{We} = \rho_o U_a^2 D / \sigma$, $\varepsilon = W/H$, $\zeta = D/H$, $\alpha = \rho_w / \rho_o$, and $\lambda = \mu_w / \mu_o$, respectively. Here, D is the diameter of the droplet, U_a is the mean channel velocity, and σ is the surface tension. The density and viscosity of water are denoted by ρ_w and μ_w, respectively, and the oil has a density ρ_o and a viscosity μ_o. The height, width, and length of the microchannel are H, W, and L, respectively.

Droplets are confined in two directions in a microchannel; thus, a three-dimensional model is necessary to consider confinement in two directions. In most existing numerical studies on the migration of particles or droplets,[8, 17, 25, 26] periodic boundaries are utilized to reduce computational cost. However, periodic boundaries significantly affect the migration of the particles[25] and tend to stabilize the particles at the outer Segré-Silberberg equilibrium positions and suppress the emergence of the inner equilibrium positions. Therefore, a full-length microchannel is used in the present numerical simulations.

The dispersed phase is Milli-Q water, and the continuous phase is hexadecane,[27] which is a commonly used combination in droplet microfluidics. Because a surfactant is often added to the microfluidic devices to stabilize the droplets, a low surface tension of 10 mN/m is set for the water/hexadecane interface. A constant axial velocity is set for the left boundary to specify the flow rate and to create a pressure-driven flow. The right boundary has an outflow condition. No-slip conditions are set for the side walls. The aspect ratio W/H is 2. The physical parameters are listed in Table I. At the beginning, the simulations proceed without droplets to obtain a steady flow field only with the continuous phase. Next, spherical droplets are initialized at certain positions and move with the carrying fluid. The longitudinal position is set to be a distance away from the inlet boundary to avoid the region where the velocity profile is under development.

C. Force measurement

The lift force experienced by a droplet can be calculated by integrating the pressure and the viscous stresses along the interface.[28] However, the lift force is difficult to accurately obtain in the current numerical framework because interfaces are implicitly presented in the VOF method. Although the interaction between a droplet and the surrounding liquid can be properly predicted, obtaining the exact forces through interpolations on an interface is still a challenge. To overcome this difficulty, we apply a constant body force to a droplet in the y or z direction to balance the lift force. Meanwhile, the droplet still moves freely with the surrounding fluid in the x direction. Thus, the lift force can be measured at a certain lateral position when the equilibrium state of the droplet is achieved. This method is similar to Stan *et al.*[19] who used buoyancy force to balance the lift forces and then achieved the measurements.

In some lateral positions, however, lift forces are difficult to measure with the above method. For example, when the body force is set to be larger than the lift force at the initial positions, the droplet will move along the direction of the body force. If the lift force decreases in that direction, the droplet will further migrate and move out of the region of interest. To address such a circumstance, we introduce a feedback forcing function developed by Suh and Lee.[29] The formulation of the feedback forces[29] acting in the y and z directions per unit mass is modified to be

$$F_y = \alpha(y_c - y_0) + \beta V + \gamma \int_0^t (y_c - y_0)dt, \tag{7}$$

$$F_z = \alpha(z_c - z_0) + \beta W + \gamma \int_0^t (z_c - z_0)dt. \tag{8}$$

Here, F_y and F_z are the body forces uniformly applied on the droplet. The droplet centroid is located at (y_c, z_c) in the cross section of the microchannel. The prescribed position is (y_0, z_0). The mean velocities of the droplet along y and z directions are V and W, respectively. The coefficients, α, β, and γ, have negative gains of the feedback forcing formulation. The feedback forces adjust themselves dynamically to bring the droplets to the prescribed position. The coefficients used in the present paper are set to be 10, 5, and 5 according to the stability analysis of Suh and Lee[29] and the time-step in our simulations. By adding the feedback forces as source terms to the momentum equation, the droplet can be driven to y_c or z_c in the y or z directions after achieving an equilibrium state. The lift force experienced by the droplet can then be obtained.

D. Grid independence study

Three cases are performed to analyze the effect of grid resolution on the computational accuracy for $\alpha = 0.77$, $\lambda = 0.33$, $\zeta = 0.6$, Re = 6.12, We = 1.5, and $\varepsilon = 2$. Droplets are released at $y/H = 0.6$ and $z/H = 0$. The background grid size is set to be $H/8$ for all the cases. The grids along the droplet interfaces are refined through a gradient-based refinement for the volume fraction to three different resolutions. The equivalent numbers of cells in one diameter, $D/\Delta x$, are 9.6, 19.2, and 38.4, respectively. The equilibrium y position increases slightly with the increasing grid resolution and the predicted equilibrium positions are $0.427H$, $0.474H$, and $0.478H$, respectively. Therefore, the highest grid resolution is sufficiently accurate to be used in the remainder of this paper.

III. EXPERIMENTAL SETUP

Experiments are carried out for comparison with the simulation results. A flow-focusing microfluidic device is designed following the work of Stan *et al.*[17] and is used to generate monodisperse droplets (as shown schematically in Figure 2(a)). After formation, the droplets are directly introduced into a rectangular channel with dimensions of 100 μm $\times$ 50 μm ($W \times H$). A side channel is introduced at approximately 600 μm after droplet generation to push the droplets toward the side wall to investigate the effect of the initial position. The length of the straight channel is 2 cm, which is long enough to obtain steady suspension.

The microfluidic device is fabricated using a standard soft lithography[14, 30, 31] technique by patterning SU8-2050 (MicroChem Corp., USA) on a silicon wafer (CapitalBio Corp., China). Polydimethylsiloxane (PDMS) mixed with the curing agent (Sylgrad184, Dow Corning Inc., USA) in a ratio of 10:1 is cast over the fabricated wafer and baked at 80 °C for 2 h after degassing. The PDMS mold is then diced and peeled from the wafer. The inlets and outlets are punched using a needle with a flattened tip. Plastic tubes are inserted into the ports and sealed with adhesive glue (3145 RTV, Dow Corning Inc., USA). The slab is then bonded to a glass substrate (25 mm $\times$ 75 mm) after an oxygen plasma treatment. Finally, the assembled device is placed into an oven at 80 °C overnight to restore the material to its native hydrophobic condition. The images of the microfluidic device are shown in Figures 3(b) and 3(c) for with and without plastic tubes. Water with red food dye is filled into the microchannel only here for visualization.

The microfluidic device is mounted on the stage of an inverted microscope (Nikon Eclipse Ti, Japan). The continuous and dispersed phases are hexadecane (Sigma-Aldrich, USA) and Milli-Q water, respectively. Span 80 (0.05% in volume, Sigma-Aldrich, USA) is dissolved in hexadecane, which reduces the hexadecane/water surface tension from 50 mN/m to 10 mN/m, as measured using the pendant droplet method (Theta tensiometers, Attension, Finland). According to Campanelli and Wang,[32] the concentration of the surfactant is below the critical micelle concentration (CMC). Hexadecane and water are introduced into the channel using three syringe pumps (Pump 11 Elite, Harvard Apparatus Inc., USA). The motion of droplets in the microchannel is recorded using a Phantom v7.3 high-speed camera (Vision Research Inc., USA) and Phantom Camera Control software. All high-speed videos are taken at a 3000 fps (frames per second) sample-rate and with a 9 μs exposure time. The captured images are analyzed with the ImageJ software package (http://rsb.info.nih.gov/ij/).
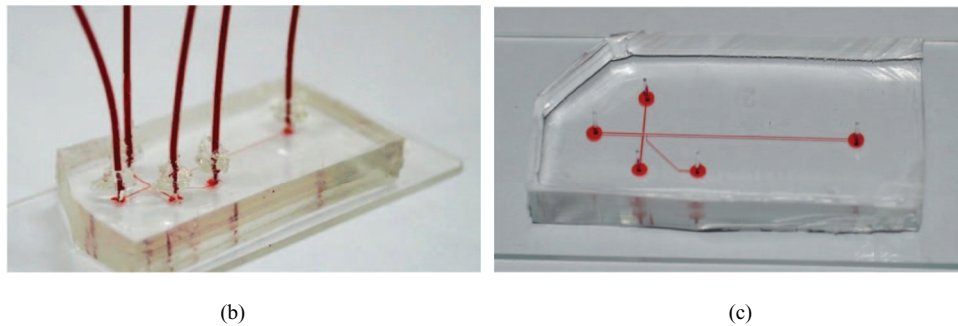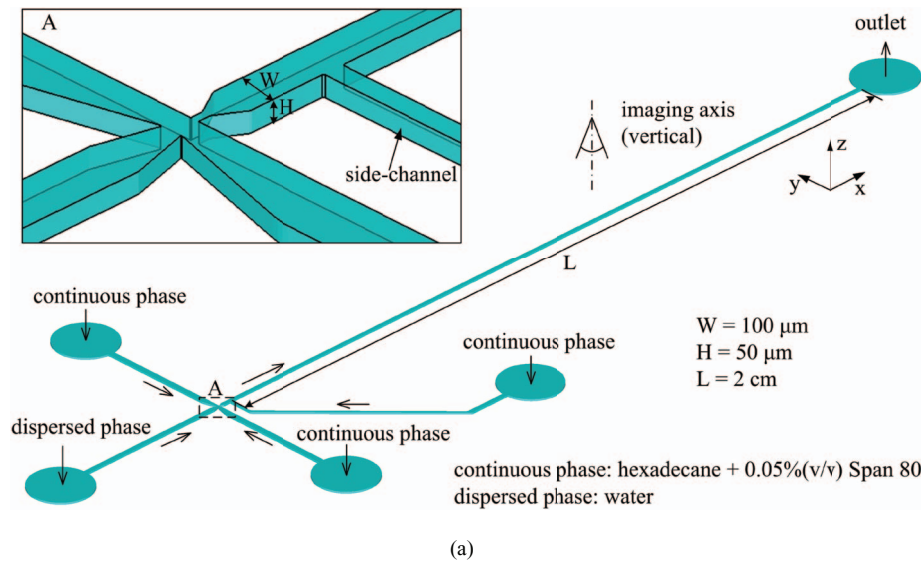
FIG. 2. Experimental setup. A long, straight microchannel for droplet migration is connected to a flow-focusing microfluidic device for droplet generation. (a) Schematic diagram. (b) Image of the microfluidic device with plastic tubes. (c) Image of the microfluidic device without plastic tubes.

IV. THEORETICAL ANALYSIS

A. Lift force

Most theoretical studies on inertial migration were based on the method of asymptotic expansion for small spherical particles.[6,33–37] Among these, a study by Ho and Leal[6] shows that the lateral
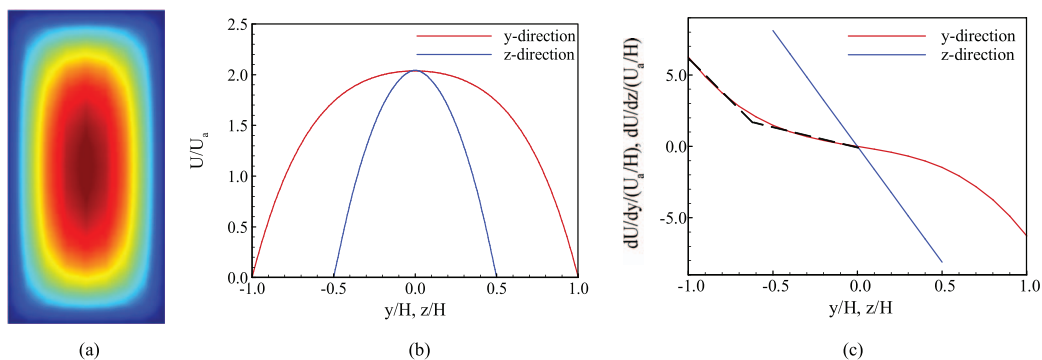

FIG. 3. (a) Contour of the velocity filed U(y, z) for the Poiseuille flow in the microchannel with an aspect ratio of 2. (b) Profiles of U along the y direction in the $z = 0$ plane and along the z direction in the $y = 0$ plane. (c) The profiles of the shear rates for the velocity profiles in (b).

force originates from the shear field acting on the small spherical particles rather than the presence of a wall-induced lag velocity or the slip-spin mechanism reported by Rubinow and Keller.[38] Ho and Leal[6] have studied both simple shear flow and two-dimensional Poiseuille flow to determine the importance of the velocity profile. The closed-form solutions for the lateral force of neutrally buoyant spheres were in good agreement with experimental observations in terms of equilibrium positions and trajectories of migrations.[39–41] The general form[6] of the lift force indicated that the interaction of the disturbance stresslet and its wall correction with the bulk shear produces a force toward the centerline, while the interaction between the stresslet and the curvature of the bulk velocity profile tends to cause migration in the direction of increasing (absolute) shear rate, where the stresslet is the symmetric first moment of the surface stress of a body in a flowing fluid.

Ho and Leal[6] highlighted that the force toward the centerline is proportional to the square of the shear rate, whereas the force toward the wall is proportional to the product of the shear rate and the curvature. The general expression of the lateral force developed by Ho and Leal[6] is applicable to all undisturbed flow fluid of the form of $a + bs + cs^2$, where s is a coordinate that varies from 0 to 1. Although the theory of Ho and Leal[6] was developed for small Re and small D, we can still utilize it to obtain a basic understanding of the effect of the velocity distribution on the lateral force. This leads us to analyze the velocity distributions in the two directions.

Figure 3(a) shows the contour of the undisturbed velocity field on the cross section with an aspect ratio of two, obtained from numerical simulations. The distributions of U/U_a are independent of Re over the range in our study (from 1.93 to 19.3) for undistributed flow. The velocity profiles along the y direction in the $z = 0$ plane and along the z direction in the $y = 0$ plane are plotted in Figure 3(b). The profile in the z direction is approximately a parabolic curve, which is a typical shape for laminar flow. In contrast, the profile in the y direction is approximately a quartic curve. The shear rate of the flow can be obtained through the derivative of the velocity profile. The absolute value of the undisturbed shear rate in the z direction increases linearly from the center to the wall (Figure 3(c)), whereas the absolute shear rate in the y direction slowly increases from the center and rapidly near the wall. The curve of shear rate in the y direction can be approximately fitted into two straight lines (shown in Figure 3(c) with dashed lines). This means that the quartic distribution of axial velocity in the y direction can be approximately divided into two parabolic regions.

Using the above finding, the quartic velocity profiles in y direction can be fitted to two parabolic curves (Figure 4(a)). Then the theory of Ho and Leal[6] developed for parabolic velocity profile can be used for the quartic velocity profile in y direction. The expression for the lateral force is[6]

$$F_l/(\rho_o U_a^2 D^4/16W^2) = (U_{max}/U_a)^2[(b + 2cs)^2 G_1(s) + (bc + 2c^2 s)G_2(s)], \qquad (9)$$

where the functions $G_1(s)$ and $G_2(s)$ are independent of the detailed undisturbed flow and were evaluated numerically for various values of s by Ho and Leal.[6]
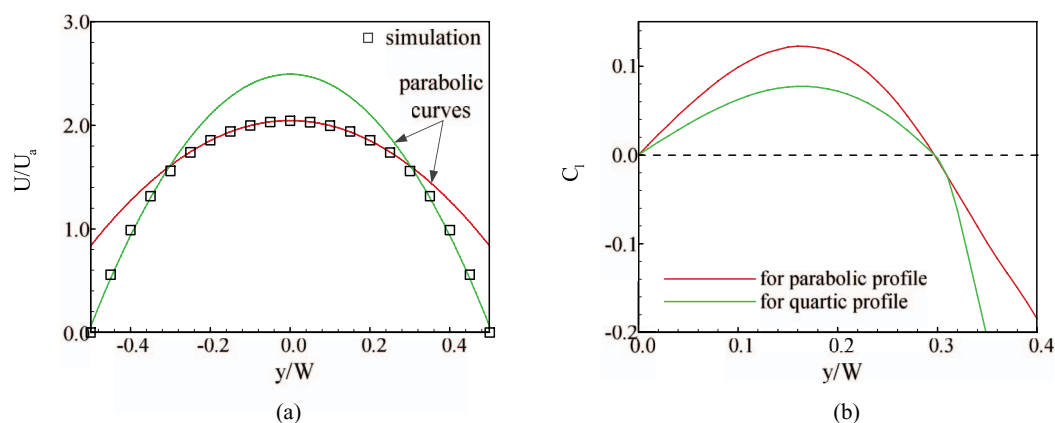

FIG. 4. (a) Two fitted parabolic curves for the velocity data in the y direction. (b) Predicted lift coefficient in the y and z directions across the centerline of the microchannel based on the theoretical analysis of Ho and Leal.[6]

Using the above theoretical expression, the lateral forces for $D/W = 0.3$ in parabolic and quartic flows are compared in Figure 4(b), where the lift coefficient C_l is defined as

$$C_l = \frac{F_l}{\pi/8\rho_o U_a^2 D^2}. \tag{10}$$

The lift coefficient of the quartic flow is obtained through the two parabolic curves. The junction of the two curves for the quartic flow is smoothed at $y/W = 0.3$. The absolute value of C_l of the quartic flow is smaller near the center and larger near the wall relative to that of the parabolic flow. The lift coefficient is zero at the centerline and is called an unstable equilibrium position.[42] Because the gradient of the force is non-zero, a small disturbance can drive a droplet away from the centerline and toward the wall. Interestingly, the stable zero-lift positions for the two velocity profiles coincide at the same scaled position $y/W = 0.3$. This means that although there are differences between the velocity profiles, the scaled equilibrium positions are the same. This finding will be validated by numerical simulations in Sec. V D.

B. Angular velocity

The rotation of a suspended droplet in the ambient liquid can be quantified by the mean angular velocity of the droplet. Different from a rigid particle, a droplet experiences deformation and internal recirculation. In order to simplify the modeling of angular velocity, the droplet is assumed to maintain a spherical shape. The velocity distribution inside the droplet is affected by the internal recirculation. However, the effect of internal recirculation is small according to our simulation results in Sec. II D. In the frame of the wall, the streamlines are only affected a little by the internal recirculation of the droplet. The axial velocity near the center of the droplet is also slightly higher than the undisturbed axial velocity due to the inner recirculation (the largest disparity is only about 7%). Therefore, in the present study, the velocity distribution inside the droplet can be considered to be the same as the undisturbed flow in the frame of the microchannel. This assumption allows us to develop a simple model to consider the effect of velocity profile on the mean angular velocity of the droplet.

Figure 5 shows the front and top views of a three-dimensional droplet in the microchannel. First, a droplet with its centroid at any y position y_0 in the $z = 0$ plane is considered (Figure 5(a)). The angular momentum with respect to y_0 of an element with a thickness of dy at y_a can be expressed as $\rho_w \pi (D^2/4 - (y_a - y_0)^2) U_y^a (y_a - y_0) dy$, where U_y^a is the averaged axial velocity of the element. Because the droplet is spherical, the distribution of the axial velocity in the y plane needs to be considered to determine the value of U_y^a. In the top view (Figure 5(b)), a similar discretization as in Figure 5(a) can be performed to obtain an expression for U_y^a as follows:

$$U_y^a = U_y \int_{-r}^{r} \left(2\sqrt{r^2 - z^2}(1 - 4z^2/H^2)/\pi r^2\right) dz, \tag{11}$$
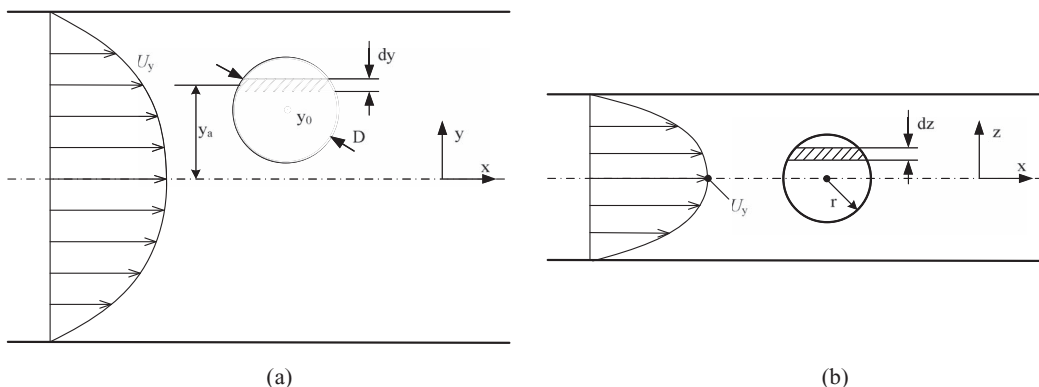

FIG. 5. Schematic diagrams for the modelling of the angular momentum of the droplets. (a) Front view. (b) Top view.

where U_y is the velocity of the undistributed flow and $r = \sqrt{(D/2)^2 - (y_a - y_0)^2}$ is the radius of the element in Figure 5(a). The parabolic profile of the axial velocity in the z direction is used in the above equation. The resultant expression for U_y^a is

$$U_y^a = U_y[1 - (D/2)^2 + (y_a - y_0)^2]. \tag{12}$$

The velocity profile in the y direction in the $z = 0$ plane for a microchannel with an aspect ratio of 2 can be expressed as

$$U_y = a + b y_a^2 + c y_a^4. \tag{13}$$

The angular momentum with respect to y_0 of the droplet can then be given as

$$L = -\rho_w \pi \int_{y_0 - D/2}^{y_0 + D/2} ((D/2)^2 - (y_a - y_0)^2) U_y^a (y_a - y_0) dy. \tag{14}$$

The final form of the angular momentum is

$$L = \rho_w \pi D^5 y_0 [6b(D^2 - 7) + c(12 D^2 y_0^2 - 84 y_0^2 + D^4 - 9 D^2)]/2520. \tag{15}$$

An expression of the angular momentum in the z direction can be obtained by the integration from the top view. The droplet centroid is set to be at any z position z_0 in the $y = 0$ plane. Because the droplet is much smaller than the height of the microchannel and because the variation of the velocity along the y direction is small near $y = 0$, the velocity distribution inside the droplet is assumed to be independent of the y position. Due to the known parabolic velocity profile in the z direction, the expression of the angular momentum reduces to a much simpler form:

$$L = 2\rho_w \pi U_a D^5 y_0/(15 H^2). \tag{16}$$

Because the rotational inertia of a droplet is $I = \rho_w \pi D^5/60$, the averaged angular velocity can then be given as $\Omega = L/I = 8 U_a y_0/H^2$, which is independent of the droplet diameter in a parabolic flow. Knowing that the shear rate in the parabolic flow is $\dot{\gamma} = -16 U_a y_0/H^2$, we find that $\boldsymbol{\Omega} = -\dot{\gamma}/2$. The right term is the angular velocity of the undistributed flow at the point of the droplet centroid, which can be expressed as Ω_f. Through derivations of Stokes' equations, Brenner[43] showed that when no external torques are exerted on a small spherical particle, it rotates with the local angular velocity of the undisturbed flow at its center at sufficiently small Re. This relation between the angular velocity and the shear rate is widely accepted in existing studies to express the rotation of a freely rotating, small spherical particle.[33,44] Our simple model indicates that $\Omega = \Omega_f$ holds acceptably for droplets of any size in a parabolic flow.

The angular velocity caused by the shear distribution in the y direction is expressed as

$$\Omega = L/I = y_0[6b(D^2 - 7) + c(12 D^2 y_0^2 - 84 y_0^2 + D^4 - 9 D^2)]/42. \tag{17}$$

The above equation shows that the mean angular velocity is dependent on the droplet size. The relations between the lateral position and Ω are obtained for different droplet sizes (Figure 6(a)). Ω is equal to Ω_f for $D/H = 0$. Small disparities are found for finite droplet sizes. The slip angular velocity $\Omega - \Omega_f$ increases with droplet size (Figure 6(b)). The predicted mean angular velocity is larger than half of the flow shear rate near the centerline but smaller near the wall. The dividing points vary between $y/H = 0.5$ and 0.6. The largest disparities are near the center, between the centerline and the dividing points.

V. RESULTS AND DISCUSSIONS

The droplet centroid is initially located between the centerline ($y/H = 0.0$) and the wall ($y/H = 1.0$) in the y direction and between the centerline ($z/H = 0.0$) and the wall ($z/H = 0.5$) in the z direction. Releasing the droplets at different positions allows us to study the dynamic process of migration as well as the effect of the velocity profile on the equilibrium position.
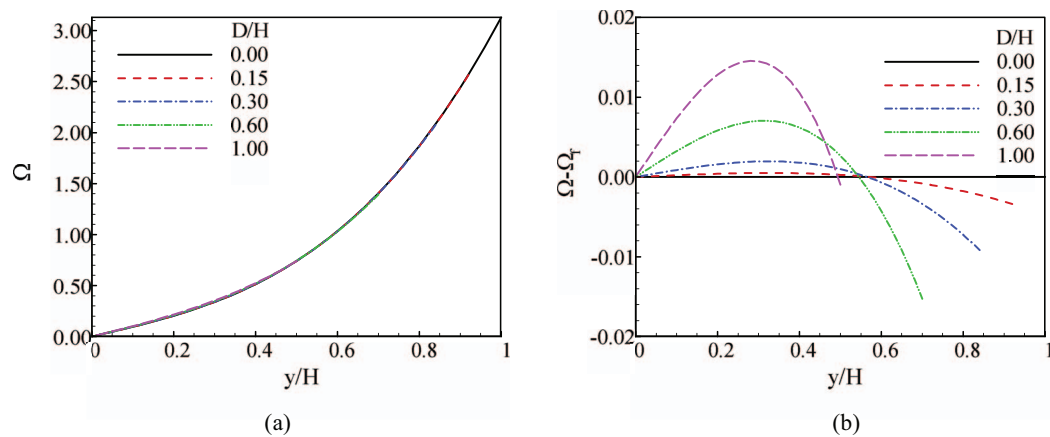
FIG. 6. Effect of droplet size on the mean angular velocity (a) and its disparity to the local shear rate (b) at different y positions.

A. Migration dynamics and deformation for a size ratio of 0.6

The migration of droplets with size ratio of 0.6 is simulated for four Re numbers in the range of 1.93–19.3. Figures 7(a) and 7(b) show the evolutions of the y positions of droplets with a size ratio $\zeta = 0.6$ released from different y positions y_i in the $z = 0$ plane for Re $= 6.12$ and 19.3. The position and time are normalized by H and D/U_a, respectively. Droplets initiated at the centerline
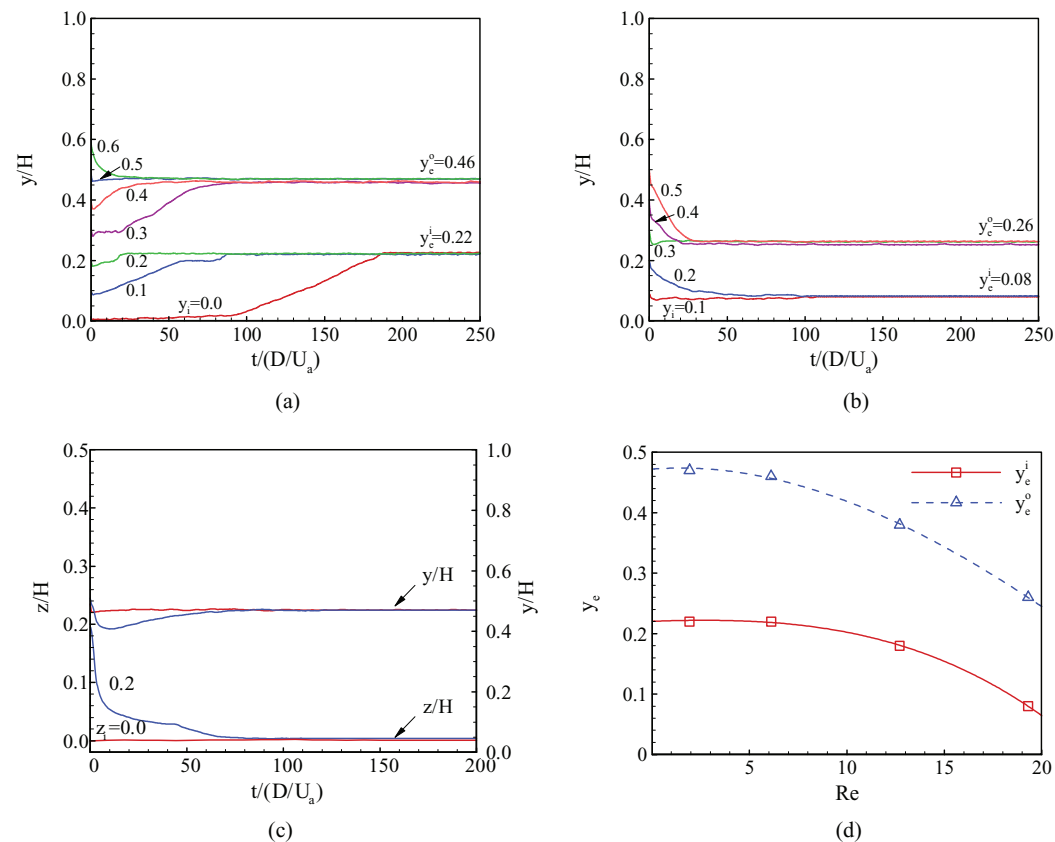

FIG. 7. Evolution of the y position of a droplet released from different positions in a microchannel for $\zeta = 0.6$. (a) Re $= 6.12$, We $= 1.5$; and (b) Re $= 19.3$, We $= 15$. (c) Comparison of droplets released at the same y position and different z positions. (d) Relations of inner and outer equivalent positions to the Re number.

of the microchannel can migrate to a positive or negative y position because of the symmetry. The trajectories with negative positions are mirrored to the positive y direction. For every Re, droplets migrate to two equilibrium y positions between the centerline and the wall, which is in contrast to previous observations of only one position for droplet migration.[8,16,17] Here, the normalized positions close to the centerline and the lateral wall are called the inner y_e^i, and outer y_e^o equilibrium positions, respectively. For Re = 6.12 (Figure 7(a)), these two positions are at $y/H = 0.22$ and 0.46, respectively. The outer position is close to the Segré-Silberberg position ($y/H = 0.6$) and is in agreement with Mortazavi and Tryggvason,[8] who showed that droplets move to approximately halfway between the centerline and the wall in a parabolic flow under a finite Re. The disagreement on the existence of the inner position may be due to the different velocity distributions. Even with similar aspect ratios, the existence of the inner position was not found during the experiments of Hur *et al.*[16] and Stan *et al.*[17] In fact, the observations of Hur *et al.* only along the y direction, and Stan *et al.*[17] have considered buoyant droplets with a negligible deformation under small Re. However, the inner position was found in experimental and numerical studies of a small spherical particle in a circular Poiseuille flow when the Re exceeded a critical value.[18,25] We will address this issue in Secs. V D–V F.

Note that there is no movement of the droplet in the z direction when released in the $z = 0$ plane. To determine if the initial z position has an effect on the equilibrium position in the z direction, an additional test is performed by releasing the droplet at $y_i = 0.5$ and $z_i = z/H = 0.2$ for Re = 6.12. The initial y position is close to the outer equivalent position to eliminate motion in the y direction. The result is compared to the case of $y_i = 0.5$ and $z_i = 0$ in Figure 7(c). The droplet released at $z_i = 0.2$ migrates to the z centerline, indicating that the force experienced by the droplet is toward the z centerline. In contrast, the variation of the y position shows a falling and subsequently rising curve because of the droplet deformation induced by the wall-induced force in the z direction. The force in the y direction increases with the deformation because the area of the acting surface increases. As the droplet moves to the centerline in the z direction, the deformation recovers, and the droplet migrates to the outer equilibrium position in the y direction.

The normalized equilibrium y positions y_e decrease with increasing Re (Figure 7(d)). The two positions for Re = 1.93 and 6.12 are nearly identical, which imply that the equilibrium positions are insensitive to the Re in the range from 1.93 to 6.12. As Re further increases, both equilibrium positions shift toward the centerline. The difference between the two equilibrium positions at the same Re decreases as Re increases.

Figure 8 shows the front, top, and side views of the droplets at the equilibrium y positions for $\zeta = 0.6$ and for different Re. Overall, the shapes become increasingly deformed with increasing Re. The deformation of the droplets in the front view is asymmetric between the top and bottom. The deformation is larger for the outer equilibrium position for each Re because the position is more influenced by the confinement. The differences of shapes between the inner and outer equilibrium positions are caused by the larger shear rate near the wall and also by the presence of the wall. Generally, the shapes change from near-round to inclined-elliptical as Re increases. The top views of the droplets become more asymmetric between the front and the rear, while they remain symmetric between the top and bottom. The shape of the droplet is similar to that of the vesicles obtained by Coupier *et al.*[45] for low Re. Negative curvature regions at the rear appear at Re = 19.3. The shapes change from near-round to bullet shaped and subsequently to parachute shaped. In contrast, the side views of the droplets become more asymmetric between the top and the bottom with increasing Re, and the shapes change from round to ellipse and subsequently to bullet shaped. Combining the different views, two types of three-dimensional shapes other than a sphere can be deduced; namely, egg shaped and parachute shaped. According to symmetry, there should be four equilibrium positions in the yz plane for each Re.

B. Migration dynamics and deformation for a size ratio of 0.3

The evolutions of the y positions and z positions of droplets for a size ratio $\zeta = 0.3$ and different Re are shown in Figures 9(a)–9(d). The droplets are released from different y positions between the centerline and the wall in the $z = 0$ plane. In contrast to the large droplets, the small droplets migrate
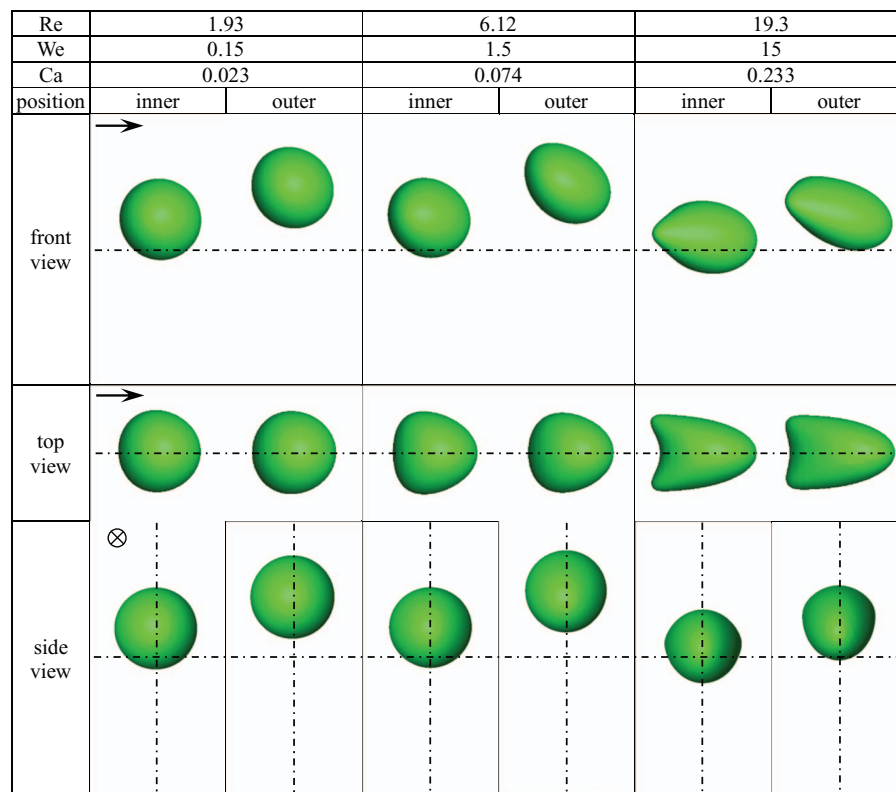
Re	1.93		6.12		19.3	
We	0.15		1.5		15	
Ca	0.023		0.074		0.233	
position	inner	outer	inner	outer	inner	outer
front view						
top view						
side view						

FIG. 8. Front, top, and side views of the equilibrium positions under different conditions at $\zeta = 0.6$. The views are along the z, y, and x directions, respectively.

in both the y and z directions. The droplets also have two equilibrium positions in the y direction for all Re. One equilibrium z position corresponds to each of the two equilibrium y positions. As shown in Figure 9(d), the differences between the equilibrium z position are small for Re = 19.3, but they are large for Re = 1.93 (Figure 9(b)). This is because the outer y equilibrium position at Re = 1.93 (Figure 9(a)) is much closer to the wall than for the other cases. The value of the shear rate in the z direction on the y plane close to the wall is much smaller. The equilibrium z position is thus close to the centerline.

Two more simulations for Re = 6.12 are carried out to test the dependence of the equilibrium position on the initial z position. The initial y position is set close to the inner equilibrium position to eliminate movement in the y direction. Figure 9(e) shows the droplets from different initial z positions migrating to the same z position. Additionally, the variations of the y position are almost the same for the three cases. This is in contrast to the cases for $\zeta = 0.6$ (Figure 7(c)) because the droplets are far away from the walls in the y direction. The deformation induced by the force in the z direction has negligible effect on the force in the y direction.

In contrast to the case of $\zeta = 0.6$, the two equilibrium y positions for $\zeta = 0.3$ decrease linearly with Re (Figure 9(f)), and the inner y position is insensitive to Re. The distance between the outer and inner y positions for the same Re decreases as Re increases. The equilibrium z positions corresponding to the inner equilibrium y positions also decrease linearly with Re.

Figure 10 shows the views of droplets at different equilibrium positions at $\zeta = 0.3$ and for different Re. The front views of the droplet for Re = 1.93 are nearly spherical, whereas a larger deformation in the top view is observed for the equilibrium z position closer to the wall. When the Re number increases to 6.12, both the front and top views of the droplets become egg-like. The deformations in the top views are larger than those in the front views. At the highest Re number (Re = 19.3), the droplet deforms to be slipper-like in the top views. The longest axes of the droplets in the front views are almost parallel to the centerline. The side views show the lateral position of
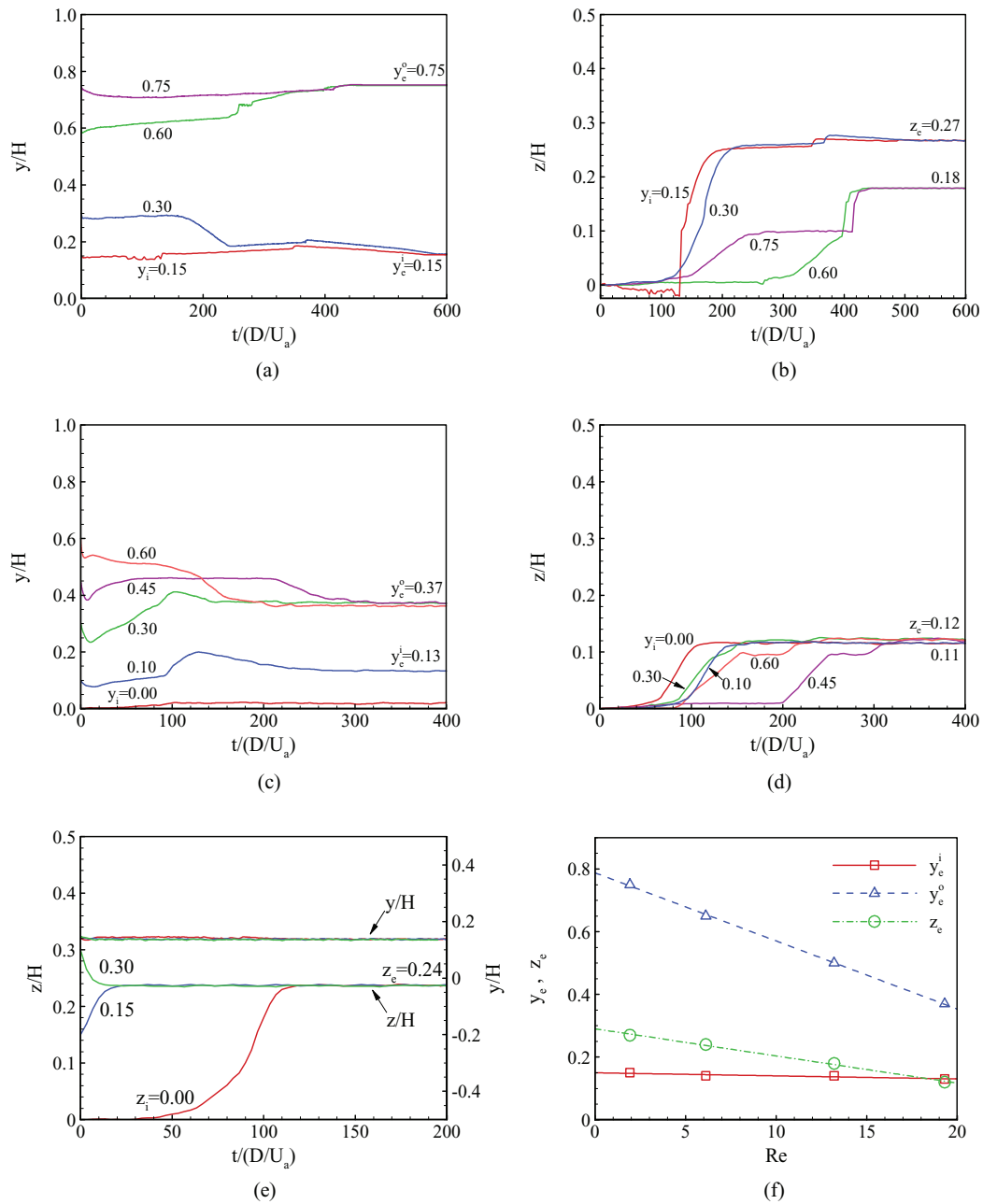
FIG. 9. Evolution of the *y* and *z* positions of a droplet released from different positions in a microchannel for $\zeta = 0.3$. (a) and (b) Re = 1.93, We = 0.15; (c) and (d) Re = 19.3, We = 15. (e) Comparison of droplets released at the same *y* position and different *z* positions. (f) Relations of equivalent positions to Re.

the droplets. According to symmetry, there should be eight equilibrium positions in the *yz* plane for each Re.

The trajectories of the positions in the *yz* plane at $\zeta = 0.3$ for different Re are plotted in Figure 11. Figure 11(a) clearly shows the two-stage evolution of the position. Taking the case of $y_i = 0.45$, for example, the droplets migrate faster in the *z* direction from the centerline to the wall in the first stage. When reaching the equilibrium *z* position, the droplet migrates faster in the *y* direction to obtain the equilibrium position as in the second stage. This is similar to the experimental observation in the particles.[46] This two-stage scenario is a result of the shear stress in the *z* direction

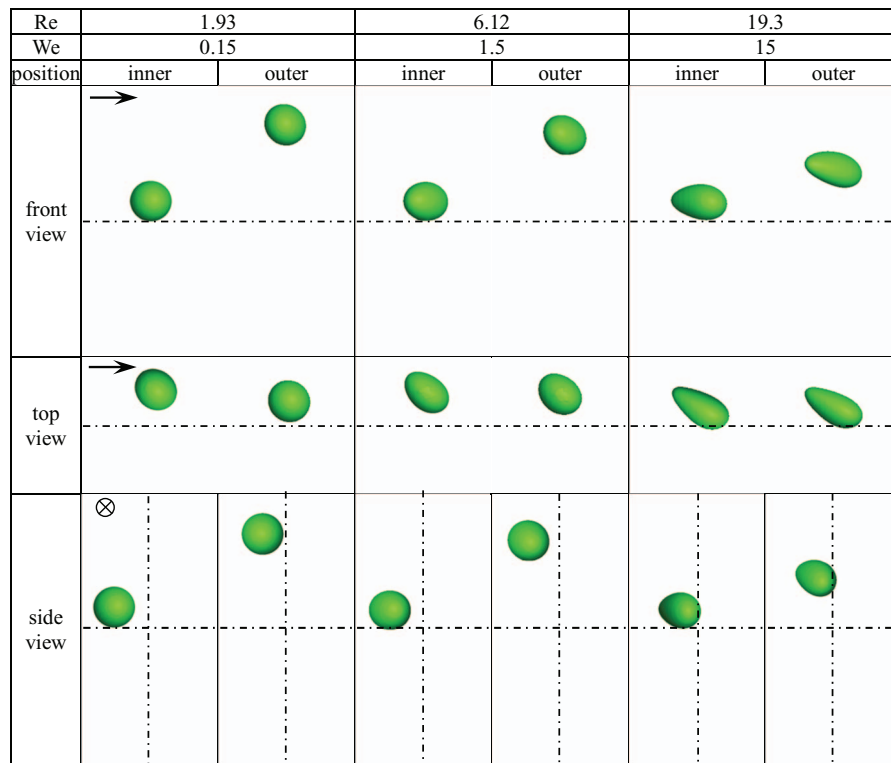| Re	1.93		6.12		19.3	
We	0.15		1.5		15	
position	inner	outer	inner	outer	inner	outer
front view						
top view						
side view						

FIG. 10. Front, top, and side views of the equilibrium positions under different conditions at $\zeta = 0.3$. The views are along the z, y, and x directions, respectively.

being larger than in the y direction as illustrated in Figure 3(c). Depending on the initial position, the two-stage scenario can be more or less observable. However, when Re is larger (as shown in Figure 11(b)), the migration speed in the two directions are comparable. The larger deformations of the droplets alter the wall-induced forces in the two directions.

C. Comparison with experimental observations

Experiments are performed to confirm the numerical findings. Figure 12(a) shows the droplet generation process at the upstream and the steady-state flows at the downstream ($x = 1.8$ cm). The
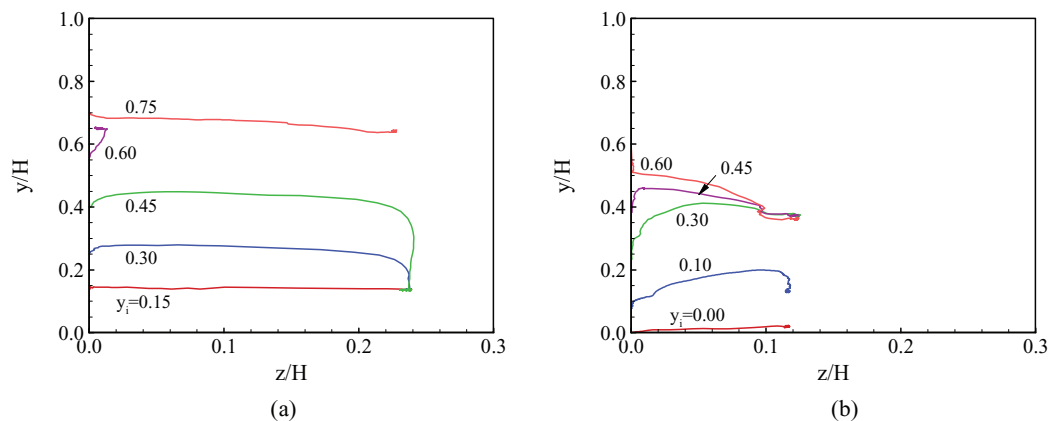

FIG. 11. Lateral position of a droplet released from different y positions in a microchannel for $\zeta = 0.3$. (a) Re = 6.12, We = 1.5; and (b) Re = 19.3, We = 15.
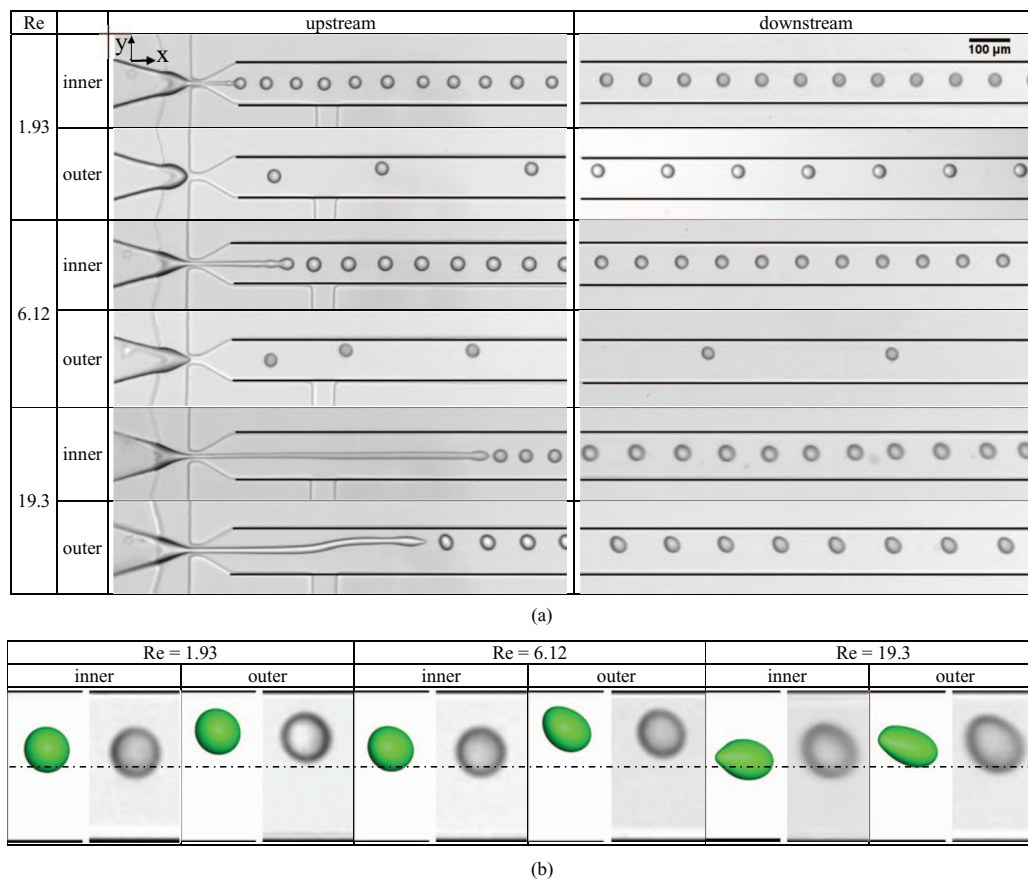
(a)

(b)

FIG. 12. (a) Experimental images from front views at the upstream and downstream of the microfluidic device for different Re. (b) Comparison between the numerical and experimental images.

total mass flow rates of the microfluidic device are controlled to match the conditions used in the numerical simulations. The droplet diameter is fixed at approximately 30 μm by adjusting the mass flow rate of the water. For each Re, two equilibrium positions are observed between the centerline and the wall. When disabling the side flows, the initial positions of the droplets are at the centerline. The droplets move slightly toward the lateral walls, and the inner equilibrium positions are obtained when the flows are steady. When enabling the side flows, the droplets are initially pushed toward the walls. The outer equilibrium positions near the wall are obtained downstream. The existence of two equilibrium positions is then validated in both the numerical simulations and the experiments.

Figure 12(b) further compares front views obtained from numerical simulations and experiments for different Re, respectively. For Re = 1.93 and 6.12, good agreements are found in terms of both the inner and outer equilibrium positions as well as the deformations. Note that the equilibrium positions in the experiments are slightly closer to the centerline. However, for Re = 19.3, although the agreements of the equilibrium positions are acceptable, the differences of the deformations are obvious. The disparities may due to the Marangoni effect, which is caused by concentration gradients in the surfactant that are not considered in the present numerical simulations. Hanna and Vlahovska[47] have shown theoretically that flow-induced surfactant redistribution on a nondeforming spherical droplet in a Poiseuille flow causes the migration of the droplet to the centerline. Numerical simulations by Janssen and Anderson[48] also illustrated that, when the droplet is close to the wall, the surfactant can be partially swept clean because of the strength of the shear flow between the interface and the wall. The deformation of the droplet can then be reduced because of dilution of the surfactant. The disparities between the numerical and experimental images shown in Figure 12(b) can then be attributed to the flow-induced surfactant dilution, which causes larger disparities with

increasing flow velocity. Note that the existing studies[47,48] on surfactant effects are limited to the Stokes flow, and further investigation is needed for the inertial migration of droplets under finite Re.

D. Effect of velocity profile on lift coefficient

Similar to particles, droplets suspended in and flowing with the surrounding flows experience pressure and viscous forces acting on the surfaces. In contrast to particles, the forces are affected by the deformation and internal flow circulation of the droplet. The wall effect and the accompanying deformation interact to alter the lift force experienced by the droplet, which makes a theoretical analysis more complicated and difficult. A quantitative understanding of the overall lift force can be addressed by the measurement of the lift coefficient at different positions. Based on the force measuring method mentioned in Sec. II C, the lift coefficients C_l at different locations are obtained for $\zeta = 0.6$ and 0.3 at Re $= 6.12$ (Figure 13).

For $\zeta = 0.6$, the lift forces are zero at three locations: the centerline and the inner and outer equilibrium positions (Figure 13(a)). As expected, there are two crests between the centerline and the outer equilibrium positions. The centerline position is an unstable equilibrium position since the lift force always drives the droplet toward the walls once the droplet departs from the centerline. The outer equilibrium position is a stable equilibrium position since the lift force always acts in the direction of driving the droplet back to the outer equilibrium position. For a droplet at the inner equilibrium position, if the droplet deviates toward the centerline, the positive lift force will drive the droplet back to the inner equilibrium position; if the droplet deviates toward the wall, the positive lift force will drive the droplet further away from the inner equilibrium position. The inner equilibrium position should then be considered a metastable equilibrium position. At the inner equilibrium position, the slope of the curve becomes zero, such that a droplet at this position is not sensitive to small disturbances. The variation of the lift force in Figure 13(a) is similar to the theoretical calculation of the lift force on a small solid particle for large Re.[37] However, the existence of the inner equilibrium position for a solid particle was not theoretically predicted. Note that the data points on the first crest are few in number because of the unstable behavior of the droplets in that region. This observation is similar to a previous study of Joseph and Ocando.[49] They determined that, for certain Re, heavier than liquid particles undergo "turning-point transitions," leading to unstable equilibrium solutions. They obtained the unstable solutions by constraining the particle in the lateral direction. However, obtaining unstable solutions for droplets is difficult because the feedback forces cannot converge at certain positions.

The lift coefficients at different z positions are obtained for $\zeta = 0.3$ and Re $= 6.12$ (Figure 13(b)). The initial y position y/H is set to be 0.15, which is the inner equilibrium y position. Body forces are only applied in the z direction, while the droplet is free in the y direction.
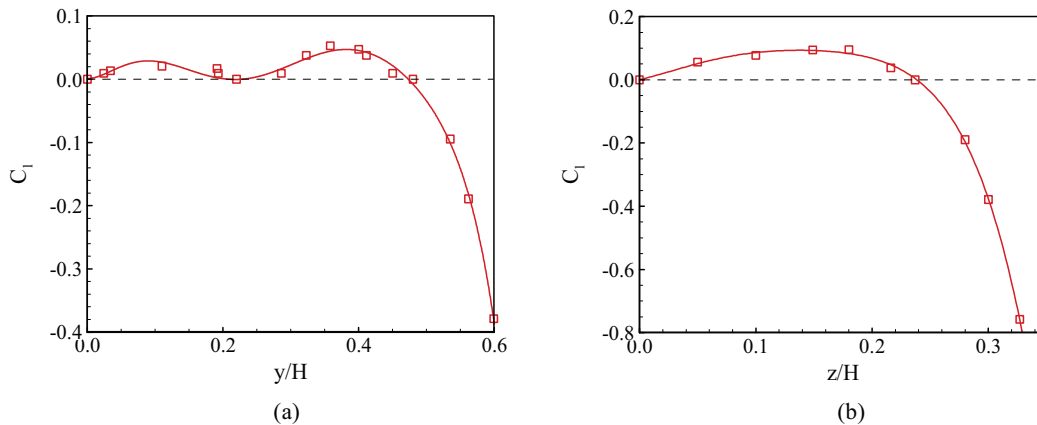

FIG. 13. Lift coefficients of droplets obtained from numerical simulations. (a) At different y positions for $\zeta = 0.6$ and Re $= 6.12$. (b) At different z positions for $\zeta = 0.3$ and Re $= 6.12$.
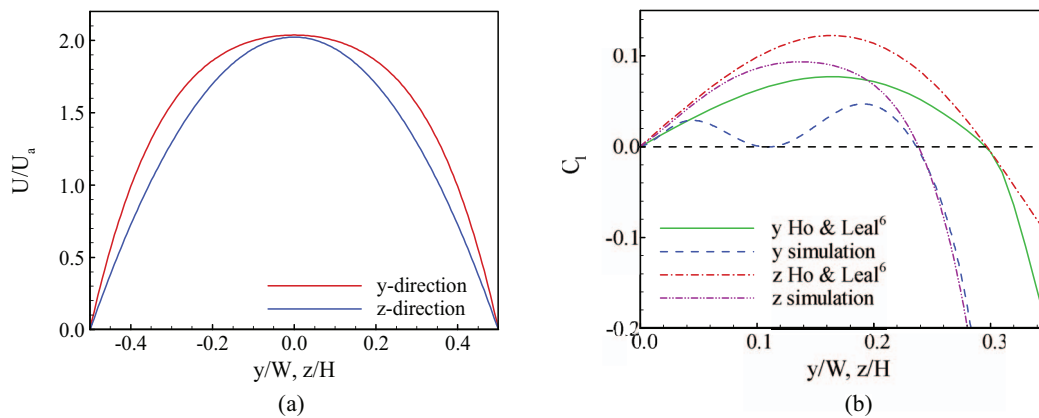
FIG. 14.   (a) Profiles of U along the y direction in the $z = 0$ plane and along the z direction in the $y = 0$ plane. (b) Comparisons of lift coefficient curves obtained from modeling and simulations for $\zeta = 0.6$ and Re = 6.12 and at different z positions for $\zeta = 0.3$ and Re = 6.12.

During each simulation, there is no motion of the droplet centroid in the y direction, which again proves that the inner equilibrium y position is a metastable equilibrium position. The lift forces in the z direction are zero at two locations: the centerline and the equilibrium positions. There is one positive curve between the centerline and the equilibrium positions.

The force experienced by a droplet depends on the size of the droplet for a fixed dimension of the channel. The chosen droplet diameters allow us to examine the effect of the velocity profiles under the same ratio of droplet size to dimension in the acting directions of the lift force. Figure 14(a) shows the profiles of the axial velocity along the y direction on the $z = 0$ plane and along the z direction on the $y = 0$ plane. By scaling the y coordinate with W for $\zeta = 0.6$, the droplet size is equivalently reduced to that of $\zeta = 0.3$. The effects of the velocity profile are then considered for the same droplet size ratio. The two fitted curves of the lift coefficients in Figure 13 as well as the predicted curves in Figure 4(b) are compared in Figure 14(b). Good agreements between the simulation data and theoretical results are obtained near the centerline. Because the effects of the finite droplet size and deformation are not considered in the theoretical analysis developed for rigid particles, the lift coefficients are over-predicted away from the centerline. Interestingly, the scaled outer equilibrium y position for $\zeta = 0.6$ coincides with the equilibrium z position for $\zeta = 0.3$. This coincidence is well-predicted by the modeling curves, despite the equilibrium position being over-predicted. Generally, the differences between the modeled and measured lift force caused by the effects of deformation-induced force and hydrodynamic interaction of droplets with the wall. Both effects increase with the distance to the centerline. The tendency coincides to the measurements of Stan *et al.*[19] for hydrodynamic force under small Re.

E. Internal recirculation and angular momentum

In contrast to solid ellipsoidal particles that rotate in the shear flow, droplets deform into an ellipsoid shape in the shear field, but the shapes are fixed at the equilibrium states. This difference is the result of internal flow recirculation inside the droplets. The streamlines in the $z = 0$ plane at the equilibrium position are shown in Figure 15 for $\zeta = 0.6$ at different Re in reference frames moving with the droplet centroids. Internal circulations inside the droplets are generated by the shear rate in the flow as well as by the viscous stress acting on the surface of the droplets. Single counterclockwise eddies inside the droplets are observed even when the droplet is close to the centerline as shown in Figure 15(c). The centers of the vortexes are near the upside. The distance between the center of the vortex and the upside of the interface becomes larger when the droplet is closer to the wall. A larger wall-induced shear stress causes a higher rotation speed on the upside of the droplet.

The cases used in Figure 13(a) for the lift coefficients allow us to study the angular momentum of the droplets at different lateral positions. Figure 16(a) compares the analytical results of the angular
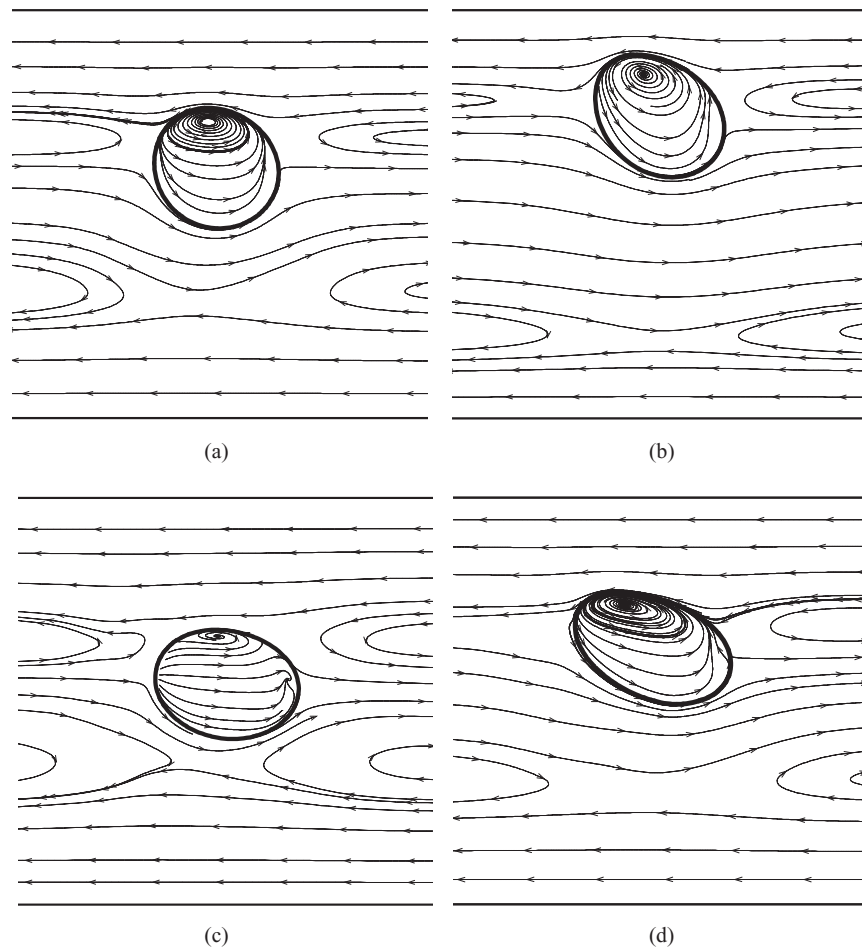
FIG. 15. Streamlines in the z = 0 plane for droplets at the equilibrium position for $\zeta = 0.6$ in a reference frame moving with the droplet centroids. Inner (a) and outer (b) positions for Re = 6.12. Inner (c) and outer (d) positions for Re = 19.3.

momentum in Sec. IV B and the measurements from the simulations for $\zeta = 0.6$ and Re = 6.12 at different *y* positions. Good agreement is found even for large deformations when the droplet is close to the wall. The predicted angular momentums are larger than the measurements. The differences between the two data appear to be nearly constant from the centerline to the wall, implying that
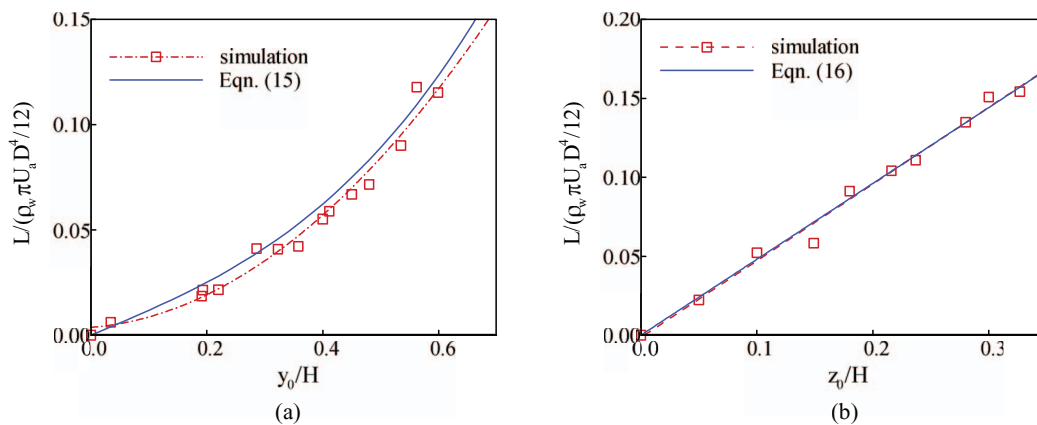

FIG. 16. Comparison of analytical modeling and numerical results of angular momentums. (a) At different y positions for $\zeta = 0.6$ and Re = 6.12. (b) At different z positions for $\zeta = 0.3$ and Re = 6.12.

the disparities are most likely caused by the shear stress from the walls in the z direction. Because the droplets are close to the walls in the z direction, the angular motions are restricted by the confinements. Figure 16(b) compares the angular momentum of the modeling and simulation for $\zeta = 0.3$ and Re $= 6.12$ at different z positions. The agreement is excellent, although there is a large deformation and confinement of the lateral wall.

F. Variation and dynamics of droplet deformation

The front views of the droplet for $\zeta = 0.6$ and Re $= 6.12$ at different y positions are shown in the top of Figure 17. The lateral positions are held by the body force while allowing deformation. Figure 17(a) shows the variation of the fluid velocity in the undisturbed flow U_f and the mean velocity of the droplet U_d at the position of the droplet centroid. The slip velocity $U_s = U_f - U_d$ slightly increases from the centerline to the wall. Taylor's deformation parameter Φ is usually used to characterize the deformation of a droplet. Taylor[50] showed theoretically that when the capillary number is sufficiently small, Φ of a slightly deformed droplet in a simple shear flow
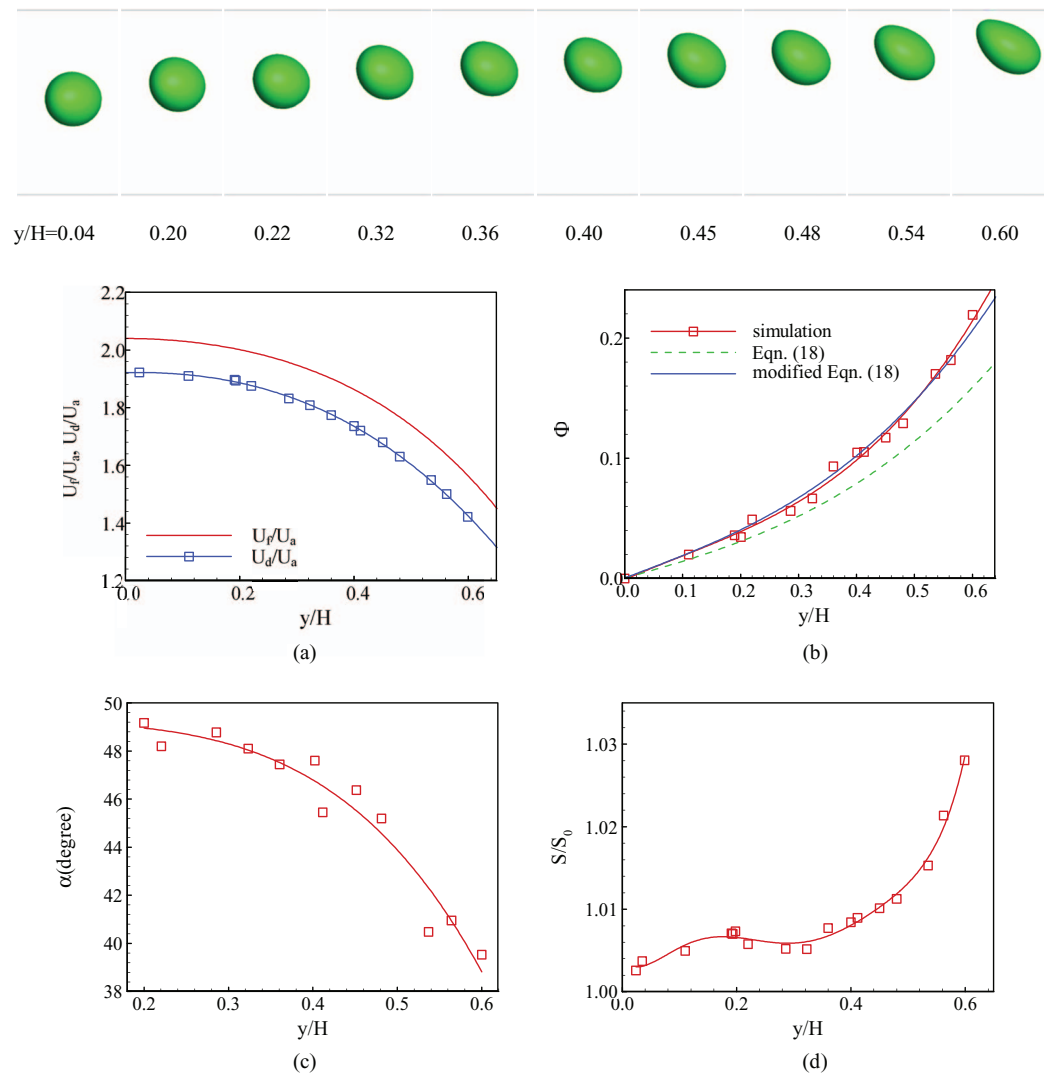

FIG. 17. Velocities (a), deformation factors (b), angle of attack (c), and surface area (d) at different y positions for $\zeta = 0.6$ and Re $= 6.12$.

can be expressed as

$$\Phi = \frac{A - B}{A + B} = \frac{19\mu_w + 16\mu_o}{16\mu_w + 16\mu_o} Ca_1,$$ (18)

where A and B are the longest and shortest axis lengths of the droplet shape, respectively. $Ca_1 = \mu_o \dot{\gamma} D / 2\sigma$ can be considered the local capillary number, which is proportional to the local shear rate. Note that the above equation is developed for flows with constant shear rates, and the effect of wall repulsion to deformation is not considered. However, we find that simply multiplying the model by a constant factor 1.296 will result in a good agreement with the simulation results as shown in Figure 17(b). Another parameter used to denote the deformation is the angle of attack α, measured from the angle between the long axis and the wall. As shown in Figure 17(c), the angle decreases from the centerline to the wall and varies around $45°$. We find that α is nearly proportional to U_f/U_a, while the ratio of their values is approximately 24.8. The change of surface area during deformation is less than 1% in the range from the centerline to the outer equilibrium position (Figure 17(d)) and can be attributed to the fact that the inertia of the droplet is comparable to its surface tension (We $\sim O(1)$). The surface area initially increases and reaches a peak value near the inner equilibrium position. After that, the surface area reduces to a minimum value at $y/H = 0.31$ and subsequently increases dramatically because of the large shear rate and wall effect.

The peak of the surface area near the inner equilibrium position indicates a larger deformation-induced force toward the centerline. Deformations should be the cause of the existence of the inner equilibrium position. The nonmonotonic variation of the surface area is most likely corresponding to that of the slip angular velocity shown in Figure 6(b). The slip angular velocity can induce additional deformation to the droplet. The predicted maximum slip angular velocity is between the centerline and the outer equilibrium position. It is also consistent with the fact that the inner equilibrium position is located between the centerline and the outer equilibrium position.

The deformations of droplets for $\zeta = 0.3$ and Re $= 6.12$ at different z positions are quantified in Figure 18. The top figure in Figure 18 shows droplets suspended from positions near the centerline to close to the wall. As shown in Figure 18(a), the difference between U_f and U_d decreases and subsequently increases slightly from the centerline to the wall. The decrease in U_s is caused by the drag force experienced by droplets decreasing with decreasing frontal area caused by deformation. The slight increase in U_s near the wall is caused by the droplets that are flattened by the wall. The drag force increases because the acting area of the shear stress along the interface increases. The deformation parameter, shown in Figure 18(b), has an increased linear tendency than that in Figure 17(b). The theoretical predication of Eq. (18) is a straight line because of the linear distribution of the shear rate (Figure 3(c)). Good agreements are found for $z/H < 0.15$. However, for $z/H > 0.15$, there are disparities that increase with z/H due to the effect of wall repulsion. Nevertheless, when multiplying Eq. (18) by a constant factor 1.273, the variation of Φ can be predicted reasonably well. Note that the constant factors for Φ in Figures 17(b) and 18(b) are close to each other. The angle of attack shown in Figure 20(c) is fitted by a parabolic curve. In contrast to $\zeta = 0.6$, the ratio of α to U_f/U_a increases from the centerline to the wall. The surface area in Figure 18(d) increases monotonically with the z position.

The evolution of the droplet deformation during droplet migration is also of interest. Following Coulliette and Pozrikidis,[51] two timescales are considered before discussing the dynamics of deformation. The deformation timescale T_{def} is the time necessary for a droplet to deform from an initial spherical shape to a nearly steady shape, and the migration timescale T_{mig} is the time necessary for a droplet to migrate a radial distance comparable to the droplet radius. The ratio of the two timescales is[51]

$$\tau \equiv \frac{T_{\text{def}}}{T_{\text{mig}}} = Ca\lambda\Phi g(\lambda)\left(\frac{D/2}{W/2 - y_e}\right)^3,$$ (19)

where $Ca = \mu_o U_a D/\sigma H$ is the capillary number and

$$g(\lambda) = \frac{3}{280}\frac{54\lambda^2 + 97\lambda + 54}{(1 + \lambda)^2},$$ (20)
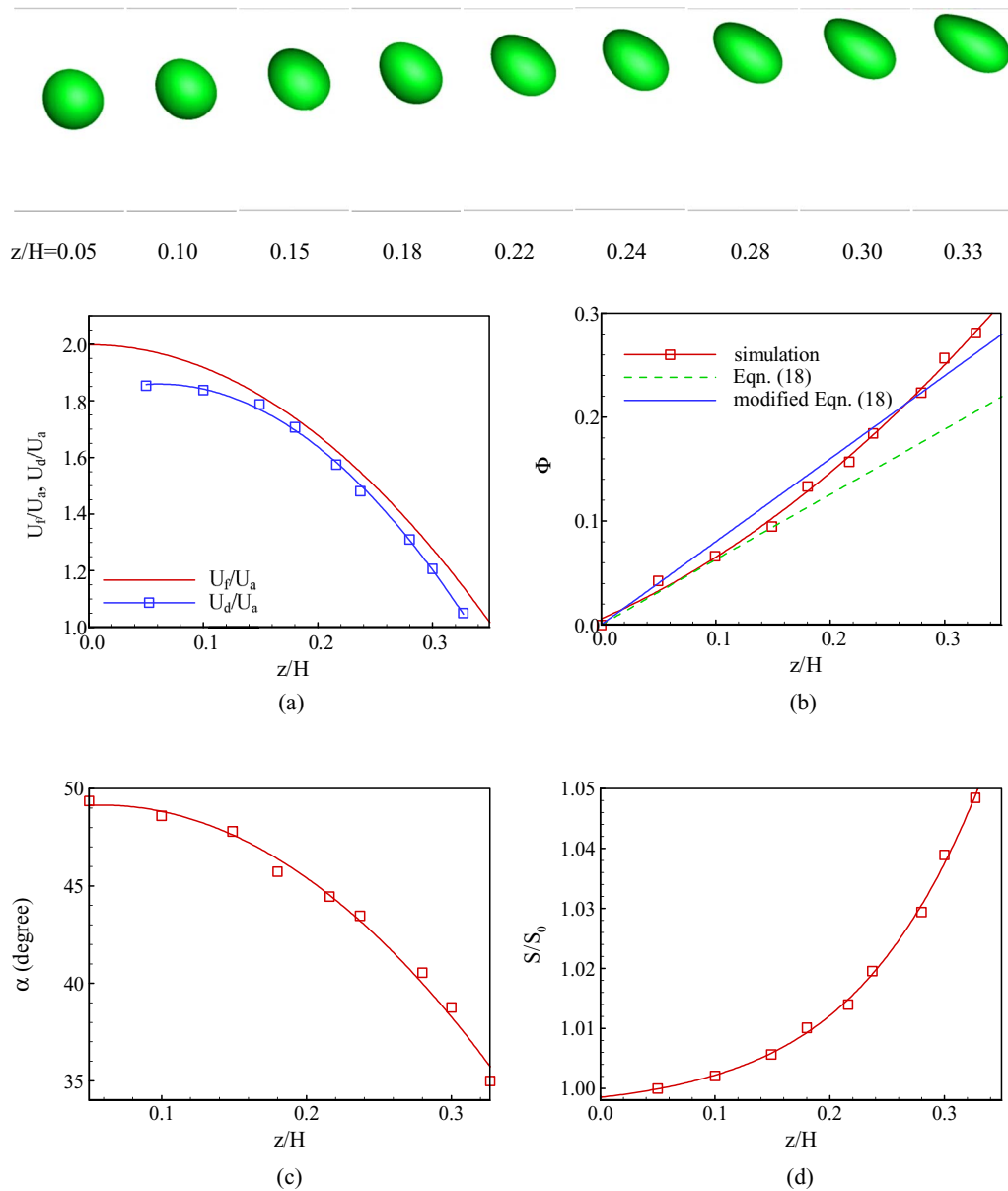
FIG. 18. Velocities (a), deformation factors (b), angle of attack (c), and surface area (d) at different z positions for $\zeta = 0.3$ and Re $= 6.12$.

which were derived by Chan and Leal.[9] In the parameter ranges considered in this paper, $Ca\lambda\Phi g(\lambda)$ is approximately $O(10^{-3})$, and the function inside the bracket is approximately $O(1)$, resulting in $\tau \ll 1$. The small value of τ means that the droplets respond rapidly to the ambient environment to change shape. Thus, the evolution of the droplet deformation can be regarded to be quasi-steady.

Figure 19 shows the evolutions of the deformation of the two droplets for different Re at $\zeta = 0.6$. The droplet in Figure 19(a) is for the case at Re $= 6.12$ with the initial released position $y_i = 0.3$. At $t/(D/U_a) = 0$, a spherical droplet is initialized in the well-developed flowfield. Due to the distribution of the velocity in the y direction, the lower region of the droplet has a higher velocity than the higher region, causing the droplet to be stretched to an ellipsoid. As it moves further downstream, the shape of the droplet changes slightly, corresponding to the balance of shear- and wall-induced lift forces. For the droplet at Re $= 19.3$ shown in Figure 19(b), the deformation of the droplet is larger and more complicated. After being initialized, the droplet is stretched by the flow to a dripping shape at
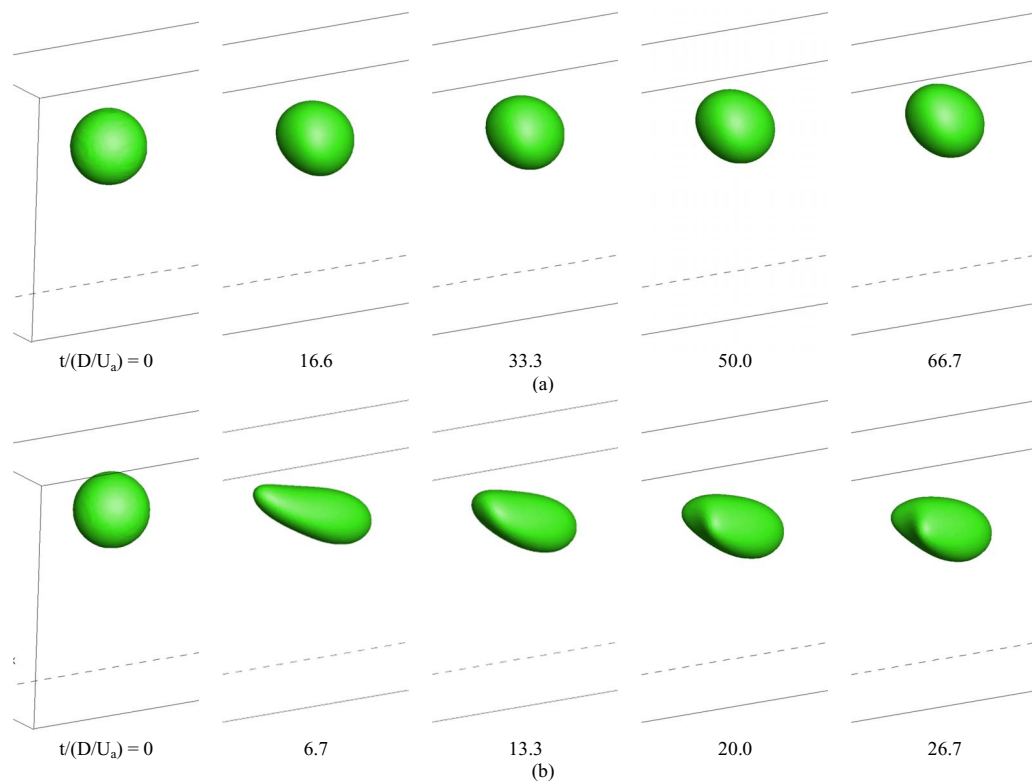
FIG. 19. Evolution of droplet shapes for different Re for $\zeta = 0.6$. (a) Re $= 6.12$, We $= 1.5$, and $y_i/H = 0.3$; (b) Re $= 19.3$, We $= 15$, and $y_i/H = 0.5$.

$t/(D/U_a) = 6.7$. The sharp tip recovers to a duckbilled shape at $t/(D/U_a) = 6.7$. As the droplet moves toward the centerline under the lift force, two tips near the wall are generated under the effect of confinement in the z direction because the shear rate in the z direction is higher toward the centerline in the y direction.

For small droplets ($\zeta = 0.3$), three-dimensional views are not able to cleanly reflect the evolution of the shapes. Front and top views are used in Figure 20. Figure 20(a) shows a case with Re $= 6.12$ and $y_i = 0.45$. The droplet migrates toward the centerline in the y direction (in the front view) and toward the wall in the z direction (in the top view). The front view of the droplet at $t/(D/U_a) = 33.3$
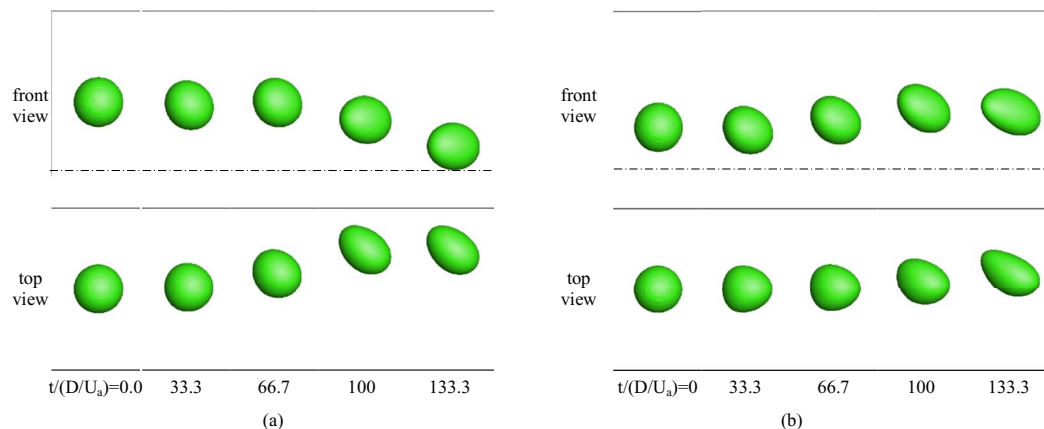

FIG. 20. Evolution of droplet shapes for different Re for $\zeta = 0.3$. (a) Re $= 6.12$, We $= 1.5$, and $y_i/H = 0.45$. (b) Re $= 19.3$, We $= 15$, and $y_i/H = 0.3$.

is an ellipsoid with a maximum axis that has an angle relative to the flow direction. As the droplet moves to the centerline, the maximum axis is approximately parallel to the flow direction because the shear rate reduces from the wall to the centerline. In contrast, the top view has a gradual variation of the droplet shape from spherical to egg-like as the droplet migrates from the centerline to the wall in the z direction. Because the deformation on the front view is small, the deformation in the two directions can be regarded as decoupled. A case for higher Re, Re = 19.3, is shown in Figure 20(b). The droplet migrates to the walls in both directions. The front view of the droplet varies from round to elliptical. During the migration in the z direction, the droplet is stretched from one angle to form a slipper shape. The irregular elliptical shape of the front view at $t/(D/U_a) = 133.3$ is due to the large deformation of the droplet in both directions.

VI. CONCLUSION

We explored the inertial migration of a single deformable droplet in a microchannel with an aspect ratio of 2. Three-dimensional numerical simulations and preliminary experiments were performed to determine the flow dynamics during droplet migration. Two types of droplets, with diameters larger and smaller than half of the channel height, were examined for three Reynolds numbers: 1.93, 6.12, and 19.3. Droplets released at different lateral positions migrate to two equilibrium positions between the centerline and the wall in the width direction and one in the height direction. The positions in both directions move to the centerline as the increasing Reynolds number causes larger deformations. Three complex, three-dimensional shapes of droplets were obtained: egg, parachute, and slipper. The lift forces experienced by droplets in the width and height directions were obtained numerically and compared with the existing theory to reflect the effects of deformation. In addition, the angular momentums of droplets with finite sizes were modeled by a simple theoretical analysis. Slip angular velocities of the droplets were found to exist in the width direction rather than in the height direction, which highlighted the effects of different velocity profiles. The evolution of the droplet deformations with the lateral positions were also studied in detail. A local extreme value of the surface area was found at the inner equilibrium position in the width direction, which reveals that the direct factor of the existence of the inner position is the altered deformation-induced force. Because the modeled slip angular velocity of the droplet has a peak near the inner position, we believe that the slip angular velocity is responsible for the extreme value of the surface area. Therefore, the existence of the inner position is attributed to the quartic profile of the axial velocity in the width direction.

[1] G. Segré and A. Silberberg, "Radial particle displacements in Poiseuille flow of suspensions," Nature **189**, 209 (1961).

[2] G. Segré and A. Silberberg, "Behaviour of macroscopic rigid spheres in Poiseuille flow part 2. Experimental results and interpretation," J. Fluid Mech. **14**, 136 (1962).

[3] R. C. Jeffrey and J. Pearson, "Particle motion in laminar vertical tube flow," J. Fluid Mech. **22**, 721 (1965).

[4] D. R. Oliver, "Influence of particle rotation on radial migration in the Poiseuille flow of suspensions," Nature **194**, 1269 (1962).

[5] A. Karnis, H. Goldsmith, and S. Mason, "The flow of suspensions through tubes: V. Inertial effects," Can. J. Chem. Eng. **44**, 181 (1966).

[6] B. Ho and L. Leal, "Inertial migration of rigid spheres in two-dimensional unidirectional flows," J. Fluid Mech. **65**, 365 (1974).

[7] P. Vasseur and R. Cox, "The lateral migration of a spherical particle in two-dimensional shear flows," J. Fluid Mech. **78**, 385 (1976).

[8] S. Mortazavi and G. Tryggvason, "A numerical study of the motion of drops in Poiseuille flow. Part 1. Lateral migration of one drop," J. Fluid Mech. **411**, 325 (2000).

[9] P. Chan and L. Leal, "The motion of a deformable drop in a second-order fluid," J. Fluid Mech. **92**, 131 (1979).

[10] H. Zhou and C. Pozrikidis, "Pressure-driven flow of suspensions of liquid drops," Phys. Fluids **6**, 80 (1994).

[11] D. Di Carlo, D. Irimia, R. G. Tompkins, and M. Toner, "Continuous inertial focusing, ordering, and separation of particles in microchannels," Proc. Natl. Acad. Sci. U.S.A. **104**, 18892 (2007).

[12] D. Di Carlo, "Inertial microfluidics," Lab Chip **9**, 3038 (2009).

[13] S. S. Kuntaegowdanahalli, A. A. S. Bhagat, G. Kumar, and I. Papautsky, "Inertial microfluidics for continuous particle separation in spiral microchannels," Lab Chip **9**, 2973 (2009).

[14] J. Sun, M. Li, C. Liu, Y. Zhang, D. Liu, W. Liu, G. Hu, and X. Jiang, "Double spiral microchannel for label-free tumor cell separation and enrichment," Lab Chip **12**, 3952 (2012).

[15] J. Sun, C. Liu, M. Li, J. Wang, Y. Xianyu, G. Hu, and X. Jiang, "Size-based hydrodynamic rare tumor cell separation in curved microfluidic channels," Biomicrofluidics **7**, 011802 (2013).

[16] S. C. Hur, N. K. Henderson-MacLennan, E. R. McCabe, and D. Di Carlo, "Deformability-based cell classification and enrichment using inertial microfluidics," Lab Chip **11**, 912 (2011).

[17] C. A. Stan, L. Guglielmini, A. K. Ellerbee, D. Caviezel, H. A. Stone, and G. M. Whitesides, "Sheathless hydrodynamic positioning of buoyant drops and bubbles inside microchannels," Phys. Rev. E **84**, 036302 (2011).

[18] J.-P. Matas, J. F. Morris, and É. Guazzelli, "Inertial migration of rigid spherical particles in Poiseuille flow," J. Fluid Mech. **515**, 171 (2004).

[19] C. A. Stan, A. K. Ellerbee, L. Guglielmini, H. A. Stone, and G. M. Whitesides, "The magnitude of lift forces acting on drops and bubbles in liquids flowing inside microchannels," Lab Chip **13**, 365 (2013).

[20] S. Popinet, "An accurate adaptive solver for surface-tension-driven interfacial flows," J. Comput. Phys. **228**, 5838 (2009).

[21] J. Brackbill, D. Kothe, and C. Zemach, "A continuum method for modeling surface tension," J. Comput. Phys. **100**, 335 (1992).

[22] S. Popinet and S. Zaleski, "A front-tracking algorithm for accurate representation of surface tension," Int. J. Numer. Methods Fluids **30**, 775 (1999).

[23] X. Chen and V. Yang, "Thickness-based adaptive mesh refinement methods for multi-phase flow simulations with thin regions," J. Comput. Phys. **269**, 22 (2014).

[24] X. Chen, D. Ma, V. Yang, and S. Popinet, "High-fidelity simulations of impinging jet atomization," Atomization Sprays **23**, 1079 (2013).

[25] X. Shao, Z. Yu, and B. Sun, "Inertial migration of spherical particles in circular Poiseuille flow at moderately high Reynolds numbers," Phys. Fluids **20**, 103307 (2008).

[26] H. Khalili and S. Mortazavi, "Numerical simulation of buoyant drops suspended in Poiseuille flow at nonzero Reynolds numbers," Acta Mech. **224**, 269 (2013).

[27] N. Bremond, A. R. Thiam, and J. Bibette, "Decompressing emulsion droplets favors coalescence," Phys. Rev. Lett. **100**, 024501 (2008).

[28] K.-I. Sugioka and S. Komori, "Drag and lift forces acting on a spherical water droplet in homogeneous linear shear air flow," J. Fluid Mech. **570**, 155 (2007).

[29] Y. Suh and C. Lee, "A numerical method for the calculation of drag and lift of a deformable droplet in shear flow," J. Comput. Phys. **241**, 35 (2013).

[30] D. C. Duffy, J. C. McDonald, O. J. Schueller, and G. M. Whitesides, "Rapid prototyping of microfluidic systems in poly(dimethylsiloxane)," Anal. Chem. **70**, 4974 (1998).

[31] J. Wang, W. Chen, J. Sun, C. Liu, Q. Yin, L. Zhang, Y. Xianyu, X. Shi, G. Hu, and X. Jiang, "A microfluidic tubing method and its application for controlled synthesis of polymeric nanoparticles," Lab Chip **14**, 1673 (2014).

[32] J. R. Campanelli and X. Wang, "Dynamic interfacial tension of surfactant mixtures at liquid–liquid interfaces," J. Colloid Interface Sci. **213**, 340 (1999).

[33] P. Saffman, "The lift on a small sphere in a slow shear flow," J. Fluid Mech. **22**, 385 (1965).

[34] J. A. Schonberg and E. Hinch, "Inertial migration of a sphere in Poiseuille flow," J. Fluid Mech. **203**, 517 (1989).

[35] A. J. Hogg, "The inertial migration of non-neutrally buoyant spherical particles in two-dimensional shear flows," J. Fluid Mech. **272**, 285 (1994).

[36] E. S. Asmolov, "The inertial lift on a spherical particle in a plane Poiseuille flow at large channel Reynolds number," J. Fluid Mech. **381**, 63 (1999).

[37] J.-P. Matas, J. F. Morris, and É. Guazzelli, "Lateral force on a rigid sphere in large-inertia laminar pipe flow," J. Fluid Mech. **621**, 59 (2009).

[38] S. Rubinow and J. B. Keller, "The transverse force on a spinning sphere moving in a viscous fluid," J. Fluid Mech. **11**, 447 (1961).

[39] J. Halow and G. Wills, "Radial migration of spherical particles in couette systems," AIChE J. **16**, 281 (1970).

[40] J. Halow and G. Wills, "Experimental observations of sphere migration in couette systems," Ind. Eng. Chem. Fundam. **9**, 603 (1970).

[41] M. Tachibana, "On the behaviour of a sphere in the laminar tube flows," Rheol. Acta **12**, 58 (1973).

[42] B. Yang, J. Wang, D. Joseph, H. H. Hu, T.-W. Pan, and R. Glowinski, "Migration of a sphere in tube flow," J. Fluid Mech. **540**, 109 (2005).

[43] H. Brenner, "Hydrodynamic resistance of particles at small Reynolds numbers," Adv. Chem. Eng. **6**, 287 (1966).

[44] D. A. Drew and S. L. Passman, *Theory of Multicomponent Fluids* (Springer, 1999), p. 184.

[45] G. Coupier, A. Farutin, C. Minetti, T. Podgorski, and C. Misbah, "Shape diagram of vesicles in Poiseuille flow," Phys. Rev. Lett. **108**, 178106 (2012).

[46] J. Zhou and I. Papautsky, "Fundamentals of inertial focusing in microchannels," Lab Chip **13**, 1121 (2013).

[47] J. A. Hanna and P. M. Vlahovska, "Surfactant-induced migration of a spherical drop in stokes flow," Phys. Fluids **22**, 013102 (2010).

[48] P. Janssen and P. Anderson, "Surfactant-covered drops between parallel plates," Chem. Eng. Res. Des. **86**, 1388 (2008).

[49] D. D. Joseph and D. Ocando, "Slip velocity and lift," J. Fluid Mech. **454**, 263 (2002).

[50] G. Taylor, "The formation of emulsions in definable fields of flow," Proc. R. Soc. A **146**, 501 (1934).

[51] C. Coulliette and C. Pozrikidis, "Motion of an array of drops through a cylindrical tube," J. Fluid Mech. **358**, 1 (1998).